



## 저작자표시-비영리-변경금지 2.0 대한민국

이용자는 아래의 조건을 따르는 경우에 한하여 자유롭게

- 이 저작물을 복제, 배포, 전송, 전시, 공연 및 방송할 수 있습니다.

다음과 같은 조건을 따라야 합니다:



저작자표시. 귀하는 원저작자를 표시하여야 합니다.



비영리. 귀하는 이 저작물을 영리 목적으로 이용할 수 없습니다.



변경금지. 귀하는 이 저작물을 개작, 변형 또는 가공할 수 없습니다.

- 귀하는, 이 저작물의 재이용이나 배포의 경우, 이 저작물에 적용된 이용허락조건을 명확하게 나타내어야 합니다.
- 저작권자로부터 별도의 허가를 받으면 이러한 조건들은 적용되지 않습니다.

저작권법에 따른 이용자의 권리는 위의 내용에 의하여 영향을 받지 않습니다.

이것은 [이용허락규약\(Legal Code\)](#)을 이해하기 쉽게 요약한 것입니다.

[Disclaimer](#)

공학박사 학위논문

**Electronic Cleansing using a  
Reconstruction Model Integrating  
Material Fractions and Structural  
Responses**

물질 혼합비율과 구조적 특징의 통합 재구성  
모델을 이용한 전자적 장세척 기법

2013년 8월

서울대학교 대학원

전기컴퓨터공학부

이 현 나

# Electronic Cleansing using a Reconstruction Model Integrating Material Fractions and Structural Responses

지도교수 신 영 길

이 논문을 공학박사 학위논문으로 제출함  
2013년 7월

서울대학교 대학원  
전기컴퓨터공학부  
이 현 나

이현나의 박사 학위논문을 인준함  
2013년 7월

위 원 장 \_\_\_\_\_ 김 명 수 \_\_\_\_\_ (인)

부위원장 \_\_\_\_\_ 신 영 길 \_\_\_\_\_ (인)

위 원 \_\_\_\_\_ 서 진 욱 \_\_\_\_\_ (인)

위 원 \_\_\_\_\_ 김 보 형 \_\_\_\_\_ (인)

위 원 \_\_\_\_\_ 이 정 진 \_\_\_\_\_ (인)

**Abstract**

**Electronic Cleansing using a  
Reconstruction Model Integrating  
Material Fractions and Structural  
Responses**

Hyunna Lee

School of Computer Science and Engineering

The Graduate School

Seoul National University

Electronic cleansing (EC) is the process of virtually cleansing the colon by removal of the tagged materials (TMs) in computed tomographic colonography (CTC) images and generating electronically cleansed images. We propose an EC method using a novel reconstruction model. To mitigate partial volume (PV) and pseudo-enhancement (PEH) effects simultaneously, material fractions and structural responses are integrated into a single reconstruction model. In our approach, colonic components including air, TM, interface layer between air and TM (air-TM interface) and interface layer between soft-tissue (ST) and TM (ST-TM interface), and T-junction (i.e., locations where air-TM interface with the colon wall) are first segmented. For each voxel in the segmented TM and air-TM interface, CT density value is replaced with the pure material density of air and thus the unexpected ST-like layers at the air-TM interface (caused by PV effect) are simply removed. On the other hand, for each voxel in the segmented ST-TM interface and T-junction, the two- and three-material fractions at the voxel are derived using a two- and three-material transition models, respectively. For each voxel in the segmented ST-TM interface and T-junction, the structural response is also calculated by rut- and cup-enhancement functions based on the eigenvalue

signatures of the Hessian matrix. Then, CT density value of each voxel in ST-TM interface and T-junction is reconstructed based on both the material fractions and structural responses to conserve the PV contributions of ST in the voxel and preserve the folds and polyps submerged in TMs. Therefore, in our ST-preserving reconstruction model, the material fractions remove the aliasing artifacts at the ST-TM interface (caused by PV effect) effectively while the structural responses avoid the erroneous cleansing of the submerged folds and polyps (caused by PEH effect). To reduce the computational complexity of solving the orthogonal projection problem in the three-material model, we currently propose a new projection method for the three-material model that provides a very quick estimate of the three-material fractions without the use of code-book, which is pre-generated by uniformly sampling the model representation in material fraction space and used to find the best match with the observed measurements. In our new projection method for the three-material model, three pairs of two-material fractions are calculated by using the two-material model and then simply combined into a single triple of three-material fractions based on the barycentric interpolation in material fraction space. Experimental results using clinical datasets demonstrated that the proposed EC method showed higher cleansing quality and better preservation of submerged folds and polyps than the previous method. In addition, by using the new projection method for the three-material model, the proposed EC method clearly reconstructed the whole colon surface without the T-junction artifacts, which are observed as distracting ridges along the line where the air-TM interface touches the colon surface when the two-material model does not cope with the three-material fractions at T-junctions.

**Keywords: Electronic cleansing, material fraction, structural response, computed tomographic colonography**

**Student Number: 2009-30208**

# Contents

Chapter 1 Introduction .....	1
1.1 Background .....	1
1.1.1 Computed tomographic colonography (CTC) .....	1
1.1.2 Fecal tagging .....	4
1.2 Problem statement of electronic cleansing (EC) .....	6
1.3 History of EC .....	8
1.3.1 Early work of EC .....	8
1.3.2 Current status of EC .....	12
1.4 Thesis contributions .....	14
1.5 Thesis outline .....	16
Chapter 2 Colon Segmentation .....	18
2.1 Overview .....	18
2.2 Anisotropic diffusion filter .....	18
2.3 Segmentation of air and TM .....	20
2.4 Segmentation of air-TM interface .....	21
2.5 Segmentation of ST-TM interface and T-junction .....	23
Chapter 3 Material Fraction Estimation .....	24
3.1 Overview .....	24
3.2 Two-material model .....	24
3.2.1 Edge transition model .....	24
3.2.2 Arch model .....	26
3.2.3 Noise isotropy .....	29
3.2.4 Orthogonal projection on the arch .....	32
3.3 Three-material model .....	34
3.3.1 Junction transition model .....	34

3.3.2	Parachute model.....	38
3.3.3	Noise isotropy .....	41
3.3.4	Orthogonal projection on the parachute.....	43
3.3.5	Fast projection based on the barycentric interpolation .....	46
Chapter 4 Structural Response .....		52
4.1	Overview .....	52
4.2	Eigenvalue signatures of folds and polyps.....	52
4.3	Structural response for folds and polyps.....	58
4.3.1	Rut-enhancement function for submerged folds .....	58
4.3.2	Cup-enhancement function for submerged polyps .....	61
Chapter 5 Reconstruction Model .....		64
5.1	Overview .....	64
5.2	Material fraction-based reconstruction model .....	64
5.3	ST-preserving reconstruction model .....	65
Chapter 6 Experiments .....		67
6.1	Dataset preparation .....	67
6.2	ST-preserving reconstruction model .....	68
6.2.1	Cleansing quality .....	68
6.2.2	Polyp detection.....	74
6.2.3	Manual cleansing measurement.....	76
6.2.4	Computational performance.....	79
6.3	Fast projection for three-material model.....	79
6.3.1	Cleansing quality .....	80
6.3.2	Computational performance.....	83
Chapter 7 Conclusion .....		85

Bibliography .....	87
초 록 .....	95
감사의 글 .....	97



## **List of Tables**

Table 4.1	Eigenvalue signatures of fold and polyp submerged in the tagged materials.....	57
Table 6.1	Grading scheme in cleansing quality evaluation.....	69
Table 6.2	Five causes for the low quality of EC .....	69
Table 6.3	Measurement results for two submerged folds in Figure 6.5 .....	77
Table 6.4	Grading scheme in comparison of cleansing quality.....	80
Table 6.5	Grading result for the perceptible difference of cleansing quality ...	83

## List of Figures

Figure 1.1	Estimated number of cancer deaths. (a) Korea in 2010. (b) The United States in 2013. ....	1
Figure 1.2	OC and CTC images. (a) A 1.4 cm polyp in the transverse colon of a 64-year-old woman. (b) A 0.8 cm polyp in the sigmoid colon of a 60-year-old man. (c) A 0.6 cm polyp in the transverse colon of a 65-year-old man. (d)-(f) The corresponding CTC images. The blue coloring indicates the part of the polyp detected by computer-aided detection (CAD) and green line indicates a portion of the colon centerline in (d)-(f).....	3
Figure 1.3	CTC performed with different bowel preparations. (a) A physically-cleansed and well-distended colon. (b) Full-cathartic preparation. (c) Reduced-cathartic preparation. (d) Non-cathartic preparation. Same contrast agent (Omnipaque 300; GE Healthcare, Princeton, NJ) was employed in the bowel preparation of (b)-(d).....	5
Figure 1.4	Example of PV artifacts. (a) A result image of segmentation by thresholding. (b) Aliasing artifacts of segmentation by thresholding. (c) A normal colonic mucosal surface without TM attached to it .....	7
Figure 1.5	Example of ST structure degradation. (a), (c) CTC images show a thin haustral fold and a small polyp ( <i>arrows</i> ) submerged in TM, respectively. (b), (d) On the cleansed CTC images obtained after a thresholding-based EC method, the thin submerged fold and polyp have erroneously been removed ( <i>arrows</i> ) .....	7
Figure 1.6	An example showing the intensity value change gradually from tissue A to tissue B. The red line represents the region boundary between tissue A and tissue B .....	10
Figure 1.7	A mixture of Gaussian distribution. The dotted lines ( <i>red</i> , <i>blue</i> , and <i>green</i> ) represent three different Gaussian distributions with different means and variances for each tissue type. The solid	

	line ( <i>black</i> ) shows a Gaussian mixture model representing an overall distribution of the observed CT density values .....	10
Figure 1.8	Example of a segmentation ray. (a) Part of a colon as seen from a traverse slice. (b) Intensity profile along the vertical scan line ( <i>yellow</i> line in (a)) .....	11
Figure 1.9	Mucosal reconstruction. (a) The stair-step scaffolding. (b) The smoothed stair-step scaffolding generated by applying a Gaussian low-pass filter. ....	11
Figure 1.10	Incomplete cleansing. (a) CTC image shows a region of inhomogeneous stool ( <i>arrow</i> ). (b) CTC image shows incomplete cleansing of the stool, leaving heterogeneous material ( <i>arrow</i> ). (c) Three-dimensional endoluminal view image shows the incompletely cleansed fecal material. <i>Green line</i> indicates a portion of the colon centerline.....	13
Figure 1.11	Process of the proposed EC method.....	16
Figure 2.1	Example of the scale-space representation. (a) $I(x, y; 0)$ at scale $t = 0$ , corresponding to the original image $I_0(x, y)$ . (b)-(d) $I(x, y; t)$ at scale $t = 1$ , $t = 4$ , and $t = 16$ .....	19
Figure 2.2	Rolling ball algorithm. (a) Ball filter with the radius of 7 voxels. (b) Magnified images at T-junction. Boundary of the ball filter touches two distinct points that respectively belong to the air ( <i>blue</i> ) and TM ( <i>green</i> ) contours. (c) Magnified images for indentation ( <i>red</i> ) that connects these two points. ....	22
Figure 2.3	Segmentation $IL_{air/TM}$ . (a), (b) Magnified images for each pair of connected air ( <i>blue</i> ) and TM ( <i>green</i> ). The ball filter ( <i>red circle</i> ) is placed tangential to each contour point of the regions. (d) Magnified images of segmented $IL_{air/TM}$ ( <i>yellow</i> and <i>red</i> ) between air and TM.....	22
Figure 3.1	Two-material transition model. (a) Ideal two-material transition	

	at $IL_{ST/TM}$ modeled by the unit-step function. (b) Blurred two-material transition at $IL_{ST/TM}$ modeled by the cumulative Gaussian distribution function..	26
Figure 3.2	Arch-shaped point-clouds for edge regions. (a) Scatter plot of intensity and gradient magnitude. (b) Scatter plot of intensity and scale-invariant gradient magnitude. Three instantiations of the arch model are superimposed corresponding to the three types of material transitions ..	27
Figure 3.3	Scale-invariant arch. (a) Scale-invariant gradient magnitude as a function of position. (b) Scale-invariant gradient magnitude as a function of density value. Single arch is obtained upon plotting the scale-invariant gradient magnitude as a function of density value ..	28
Figure 3.4	Estimation of material fractions of ST and TM using orthogonal projection on the arch.....	33
Figure 3.5	Configuration of three-material transition at a T-junction.....	34
Figure 3.6	Three-material transition model with $\alpha = 90^\circ$ . (a) Ideal three-material transition at T-junction modeled by the unit-step function. (b) Blurred three-material transition modeled by the cumulative Gaussian distribution function. (c) Gradient magnitude as a function of position. (d) Second directional derivative as a function of position..	37
Figure 3.7	Barycentric coordinate in a triangular domain $(C_{air}, C_{ST}, C_{TM})$ . (a) Image acquisition combines contributions of different materials into the partial volume CT density value. These contributions are represented as barycentric positions $(t_{air}, t_{ST}, t_{TM})$ . $I_{air}$ , $I_{ST}$ , and $I_{TM}$ represent the expected CT density values of air, ST, and TM, respectively. (b) Edges of the triangle denote mixtures of two materials, corresponding to the arches for two-material transition.....	38
Figure 3.8	Parachute projection. (a) First-order parachute function	

displaying  $\sigma_{\omega} I_{\omega}$  as function of barycentric position. (b) Second-order parachute function displaying  $\sigma_{\omega}^2 I_{\omega\omega}$  as function of barycentric position. (c) Ambiguity in the estimation of three-material fractions using the data measurement pair  $(I, \theta \sigma_{\omega} I_{\omega})$ . Probing the surface of the first-order parachute function along a fixed density (*dark line*) results in equal altitude for two positions. (d) Including the second derivative (b) in gradient direction (*dashed line*) solves this problem. This can be seen since equal gradient magnitudes have different second derivative in gradient direction.. 44

Figure 3.9 Sampling of model representation. (a), (d) Streamlines along  $\omega$  generated in barycentric space until the distance between the lines is below a certain minimum: 0.2 and 0.05 (distances in material fraction). (b), (e) Corresponding streamlines in image space. (c), (f) Artifacts from undersampling. Artificially generated polyps are used with sizes 3, 5, 7, 9, and 11 mm and  $\sigma = 1$  mm. The left part of middle polyps connects to TM and right part connects to air..... 46

Figure 3.10 Proposed parachute projection method. (a) Three arch projections of data measurement pair  $(I, \theta \sigma_{\omega} I_{\omega})$ . The positions of three arch-projection points *APs* derive three pairs of two-material fractions. (b) Barycentric interpolation in a triangular domain  $(C_{air}, C_{ST}, C_{TM})$ . When using uniform weights, barycentric point *BP* is determined as the center of the triangle formed by three *APs*. The propotion of the areas of three sub-triangles (*light grey*, *grey*, and *dark grey*) represents the three-material fractions..... 47

Figure 4.1 Morphologic shapes of a haustral fold and a colonic polyp. (a) Schematic illustration of the fold, the polyp, and the colonic wall. (b) Planar surface of the colon. The fold is depicted as a

	ridge-like structure, whereas the polyp is depicted as a cap-like structure. The three vectors $e_1$ , $e_2$ , and $e_3$ represent the eigenvectors of the Hessian matrix for the fold and the polyp.....	54
Figure 4.2	Profiles of a submerged fold on a colon phantom. (a) Two sampling lines on the cross-sectional image of a fold. (b) Coronal view of the fold in (a). (c) Plot of the change in CT density values and eigenvalues of the Hessian matrix along the short axis in (a). (d) Plot of the change in CT density values and eigenvalues of the Hessian matrix along the long axis in (a) .....	55
Figure 4.3	Profiles of a submerged polyp on a colon phantom. (a) A sampling line on the cross-sectional image of a polyp. (b) Coronal view of the fold in (a). (c) Plot of the change in CT density values and eigenvalues of the Hessian matrix along the sampling line in (a).....	57
Figure 4.4	Effect of discrimination function $F_A$ on the differentiation of folds from other structures in the colon phantom. (a) $F_A$ as a function of $R_a$ at different values of $\alpha$ . (b) Coronal view of the CTC images of a colon phantom. All voxels above 200 HU are shaded. (c) Response images of the phantom image resulting from the application of $F_A$ at $\alpha = 0.1$ , $\alpha = 0.25$ , and $\alpha = 0.5$ .....	59
Figure 4.5	Effect of discrimination function $F_B$ on the differentiation of folds from other structures in the colon phantom. (a), (b) $F_B$ as a function of $R_b$ at different values of $\beta$ and at the fixed values of $\gamma = 0.2$ and $\gamma = 0.3$ . (c), (d) Response images of the phantom image resulting from the application of $F_B$ at $\beta = 0.1$ , $\beta = 0.3$ , and $\beta = 0.5$ with $\gamma = 0.2$ and $\gamma = 0.3$ ...	61
Figure 4.6	Effect of discrimination function $F_C$ on the differentiation of	

	polyps from other structures in the colon phantom. (a) $F_C$ as a function of $R_c$ at different values of $\eta$ . (b) Response images of the phantom image resulting from the application of $F_C$ at $\eta = 0.1$ , $\eta = 0.2$ , and $\eta = 0.5$ .....	62
Figure 4.7	Demonstration of the effect of the structural enhancement functions on folds and polyps. (a), (c) Portion of the colonic lumen filled with TMs. (b), (d) Result of the structural response to the lumen in (a) and (c). The folds and polyps submerged in the TMs are well enhanced.. .....	
Figure 6.1	Comparison of 3D band view images from $EC_{prev}$ and $EC_{our}$ . (a) Band view image generated from the original dataset before EC. (b), (d) Magnified images of submerged folds from $EC_{prev}$ . (c), (e) Magnified images of submerged folds from $EC_{our}$ .....	71
Figure 6.2	Quality grades for tagged pools determined by a radiologist for 10 scans. Two bar at each scan represent $EC_{prev}$ ( <i>left</i> ) and $EC_{our}$ ( <i>right</i> ). Each gray shaded color represents different quality grades: grade 1 ( <i>black</i> ), grade 2 ( <i>dark gray</i> ), grade 3 ( <i>light gray</i> ), or grade 4 ( <i>white</i> ).. .....	
Figure 6.3	Reasons for low quality of EC. Two bar graphs represent $EC_{prev}$ ( <i>left</i> ) and $EC_{our}$ ( <i>right</i> ). Each gray shaded color represents five different reasons for the low quality of EC: artifacts at T-junctions ( <i>black</i> ), inhomogenous tagging ( <i>dark gray</i> ), collapsed segment ( <i>light gray</i> ), image noise ( <i>gray</i> ), and incomplete EC ( <i>oblique line</i> ).....	73
Figure 6.4	Comparison of 3D band view images from $EC_{prev}$ and $EC_{our}$ . (a) Band view image generated from the original dataset before EC. (b), (d) Magnified images of submerged folds from $EC_{prev}$ . (c), (e) Magnified images of submerged folds from $EC_{our}$ .....	75
Figure 6.5	Comparison of 2D slice images from $EC_{prev}$ and $EC_{our}$ . (a) Original CT image. (b) Magnified image of submerged folds	

	from $EC_{prev}$ . (c) Magnified image of submerged folds from $EC_{our}$ .....	77
Figure 6.6	Objective evaluation results for manually segmented fold regions in 10 scans. (a) Mean density values. (b) Fold preservation rates. Two bar graphs at each scan represent $EC_{prev}$ ( <i>left, gray</i> ) and $EC_{our}$ ( <i>right, black</i> ).....	78
Figure 6.7	Comparison of 3D band view images from $EC_{two}$ and $EC_{three}$ . (a) Band view image generated from the original dataset before EC. (b), (d) Magnified images of T-junctions from $EC_{two}$ . (c), (e) Magnified images of T-junctions from $EC_{three}$ . The <i>pink coloring</i> indicates the part of the electronically cleansed TM regions in (b)-(e) .....	82



# Chapter 1. Introduction

## 1.1 Background

### 1.1.1 Computed tomographic colonography (CTC)

Colon cancer is the fourth and second leading cause of cancer deaths in Korea and the United States, respectively [see Figure 1.1]. Approximately 25,000 and 150,000 new cases of colon cancer are diagnosed every year in both countries [1, 2]. Similar to other cancers, it is often diagnosed at an advanced stage, after the patient has developed symptoms. Different from many cancers, colon cancer can be prevented by detection and removal of its precursor lesion, the adenomatous polyp. Consequently, it is imperative that an effective diagnostic procedure be found to detect colonic polyps or tumors at an early stage and a periodic examination of the colon is recommended to detect and remove colonic polyps at the early stage [3, 4].

Since the first reported complete examination of the colon using a flexible fiber-

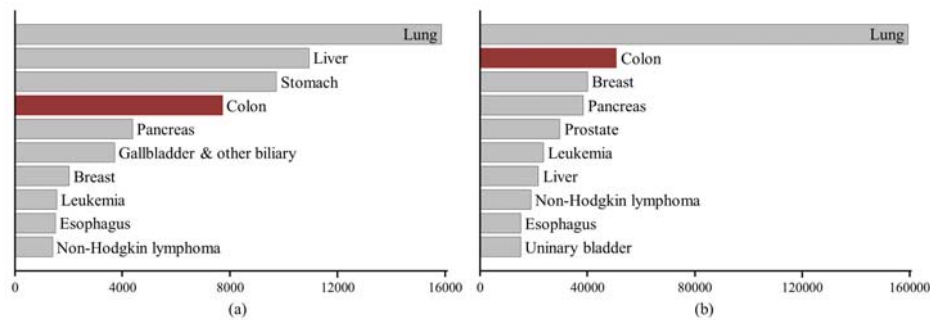


Figure 1.1 Estimated number of cancer deaths. (a) Korea in 2010. (b) The United States in 2013.

optic endoscope by Wolff and Shinya in 1971 [5], optical colonoscopy (OC) has evolved to be the current gold standard for evaluation of the entire colonic mucosal surface with therapeutic capability of resecting detected lesions [6]. However, OC is an invasive procedure, in which a fiber-optical probe is inserted into the colon through the rectum and the inner surface of the colon is examined by manipulating a small camera at the tip of the probe. Therefore, OC is uncomfortable for the patient [7] and it has several drawbacks as a screening option [8].

- It is an invasive procedure and sedation may be needed. The use of sedation requires an escort, increases the costs and may induce complications such as cardiac arrhythmias, hypotension, oxygen desaturation, and others [9].
- The bowel preparation before the procedure is stressful, requiring a full oral laxative colon cleansing, and may cause abdominal discomfort, cramps, nausea, and other symptoms [10, 11].
- OC is time-consuming, typically ranging from 30 min to an hour for the procedure and 1-2 hours recovery time.
- It carries a small risk of perforation and death (colonic perforation in 1 in ~1000 cases and death in 1 in ~5000 cases [12-14].
- It may fail to demonstrate the entire colon about 1 in 10 patients who not have a complete right colon (cecum) evaluation [15-17].

To overcome such limitations of OC, computed tomographic colonography (CTC), also known as virtual colonoscopy VC, has accepted as a promising procedure for the noninvasive screening of colon cancers [6, 18-21]. CTC utilizes computer virtual-reality techniques to navigate inside a three-dimensional patient-specific colon model reconstructed from abdominal computed tomography (CT)

images, looking for polyps. That is, CTC mimics the OC navigation procedure without the insertion of probes [see Figure 1.2] [22, 23]. Although there are several obstacles preventing CTC from becoming a complete alternative to traditional OC such as the need to follow-up OC on the positive findings, the radiation risk, the challenge in detecting small polyps, and the readers' variation, research to overcome these obstacles is underway and CTC has demonstrated the potential to become a mass screening modality, especially as a preferred approach to OC, due to its safety, lower cost, and better patient compliance than OC [20, 24-26]. In the future, a good combination of CTC screening with OC follow-up could be a cost-effective means to prevent the deadly disease.

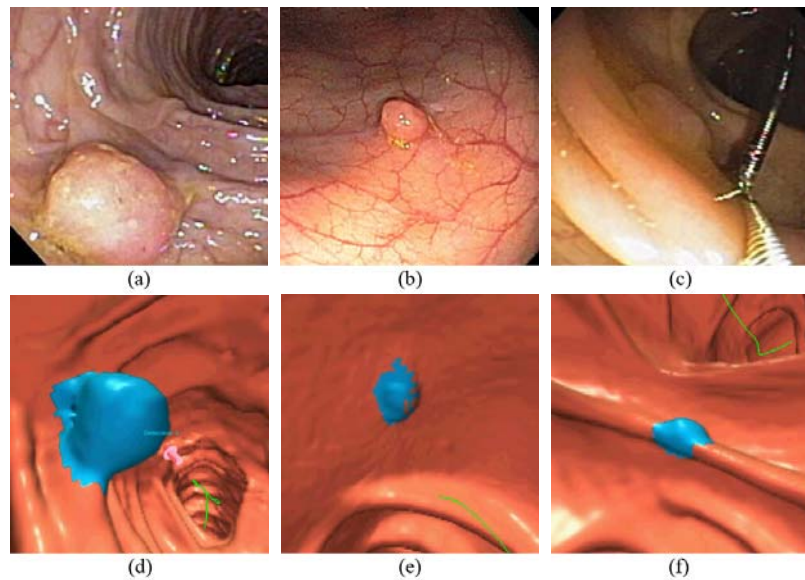


Figure 1.2 OC and CTC images. (a) A 1.4 cm polyp in the transverse colon of a 64-year-old woman. (b) A 0.8 cm polyp in the sigmoid colon of a 60-year-old man. (c) A 0.6 cm polyp in the transverse colon of a 65-year-old man. (d)-(f) The corresponding CTC images. The *blue coloring* indicates the part of the polyp detected by computer-aided detection (CAD) and *green line* indicates a portion of the colon centerline in (d)-(f).

### **1.1.2 Fecal tagging**

Similar to OC, CTC also requires a thorough bowel cleansing of the colon prior to CT data acquisition. This is because residual materials decrease the sensitivity and specificity of CTC. Due to the similarity in X-ray attenuation among colonic fluid, stool and colon wall, colonic fluid may obscure colonic polyps and adherent stool may create false-positives. Therefore, the thorough bowel cleansing has been identified as one of the major sources of poor patient compliance not only in OC but also in CTC. To circumvent this limitation, fecal tagging, which enhances residual materials using radiopaque contrast material, has been introduced [27, 28]. Since residual materials mixed with the orally administered contrast material appear hyperdense on CT scans, whitely tagged fluid and stool can be easily differentiated from untagged soft-tissue (ST) structures including colonic polyps and cancers, resulting in the increase of both the sensitivity and specificity of CTC.

Fecal tagging for CTC is often combined with a certain amount of cathartic or laxative agent, such as sodium phosphate, bisacodyl, or magnesium citrate, that draws fluid into the bowel lumen to induce peristalsis and eliminate bowel contents. There are three major types of bowel preparation for fecal tagging in CTC examination based upon the dose of catharsis applied: full-, reduced-, and non-cathartic preparation [see Figure 1.3]. Compared to full-cathartic preparation, reduced- and non-cathartic preparations accomplish relatively mild purgation while reducing and minimizing patient burden.

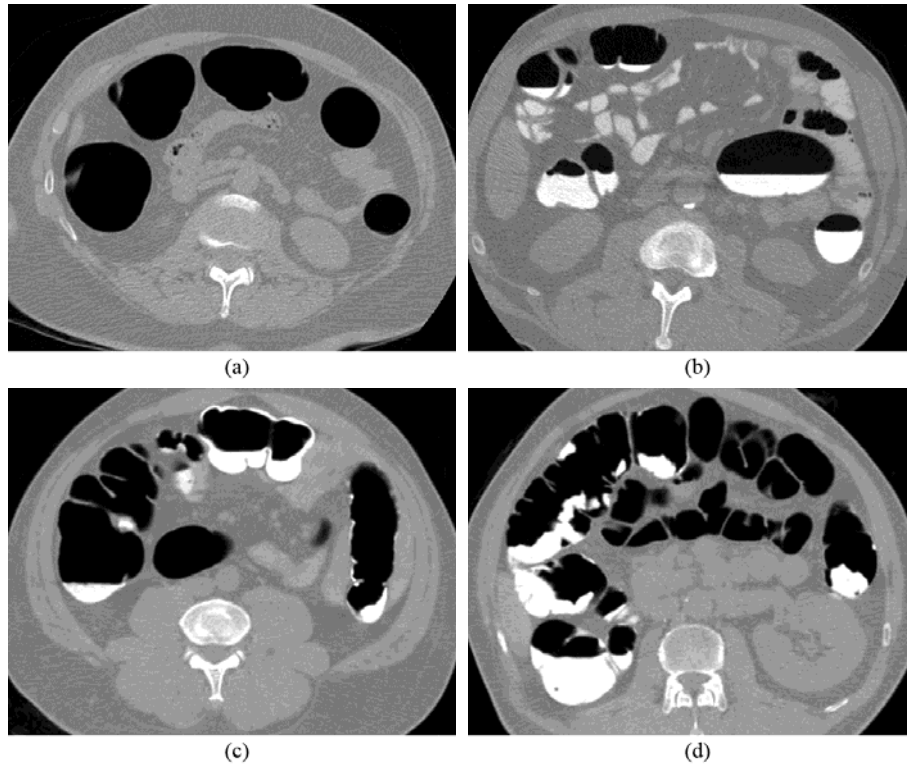


Figure 1.3 CTC performed with different bowel preparations. (a) A physically-cleansed and well-distended colon. (b) Full-cathartic preparation. (c) Reduced-cathartic preparation. (d) Non-cathartic preparation. Same contrast agent (Omnipaque 300; GE Healthcare, Princeton, NJ) was employed in the bowel preparation of (b)-(d).

The popular use of fecal tagging has led to the development of “electronic cleansing (EC)”. The goal of EC is the virtual cleansing of the colon by removal of the tagged materials (TMs) in CTC images and generating electronically cleansed images such as that shown in Figure 1.3(a).

## 1.2 Problem statement of electronic cleansing (EC)

With the use of fecal tagging, TMs can be easily segmented and subtracted based on their CT density values, because they appear hyperdense enough to be differentiated from other ST structures. However, there still are two major causes of cleansing artifacts, which is believed to impair the diagnostic utility of electronic cleansed CTC images using naïve segmentation approaches such as the thresholding and morphological operations.

First, partial volume (PV) effect generates unexpected ST-like layers at the air-TM interface as well as aliasing artifacts at the ST-TM interface. Due to the limited resolution of the CT scanner, a single voxel may represent more than a single tissue type at a time, and the measured CT density is dependent on the individual tissue densities and the volume ratio of the tissues within the voxel. At the boundary of two regions with different densities, voxels have CT densities that do not match either of the two regions and they are incorrectly classified when thresholding is used. When thresholding removes the high density TM voxels, the PV voxels at the air-TM interface are miss-classified as ST voxels and not removed, resulting in an unexpected thin ST-like layer, which is not present in reality. In addition, thresholding also gives rise to aliasing artifacts at the ST-TM interface. Because of PV effect, the normal transition from air regions to ST regions of the bowel wall typically shows slowly varying densities. However, simple subtraction generates an unnaturally rapid transition from the subtracted TM regions to ST regions. The rapid transition at the ST-TM interface results in a visually distracting, artificial texture of the inner colon wall. Figure 1.4 illustrates an example of PV artifacts.

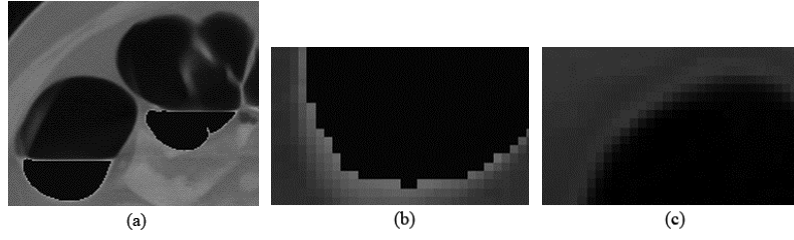


Figure 1.4 Example of PV artifacts. (a) A result image of segmentation by thresholding. (b) Aliasing artifacts of segmentation by thresholding. (c) A normal colonic mucosal surface without TM attached to it.

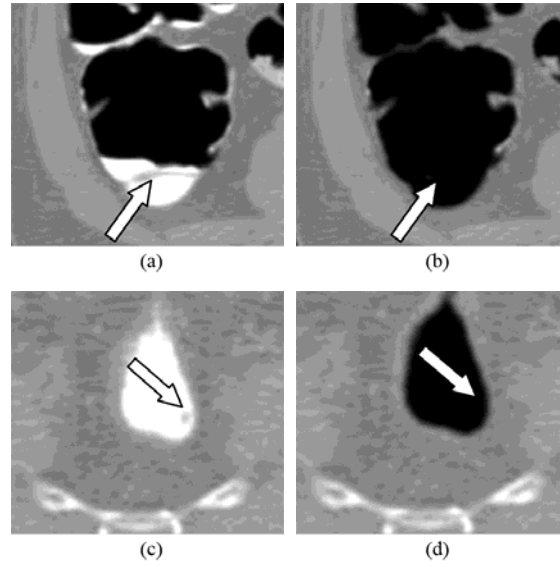


Figure 1.5 Example of ST structure degradation. (a), (c) CTC images show a thin haustral fold and a small polyp (*arrows*) submerged in TM, respectively. (b), (d) On the cleansed CTC images obtained after a thresholding-based EC method, the thin submerged fold and polyp have erroneously been removed (*arrows*).

Second, pseudo-enhancement (PEH) effect causes ST structure degradation. Fecal-tagging agents that are used for enhancing residual materials to facilitate their confident differentiation from colonic polyps tend to artificially elevate the observed CT density of voxel nearby TMs toward that of TMs. When folds

and polyps are submerged in or partially covered by the TMs, due to the presence of adjacent high density TMs, they are miss-classified as TMs and thus erroneously removed, resulting in degraded or eliminated folds or polyps. Figure 1.5 illustrates the problems introduced by the PEH effect.

## **1.3 History of EC**

### **1.3.1 Early work of EC**

Since the term EC was first introduced by Wax and Liang [29], various EC approaches utilizing image segmentation and pattern recognition algorithms have been investigated over the last decade [4, 30-39]. At its early stage, EC was designed to the removal of TMs in the full-cathartic fecal tagging CTC based on the following EC assumptions:

- TM appears as a bowl-shaped liquid pool located at the bottom of the colonic lumen due to the gravitational effect.
- TM has a large, flat, and horizontal surface contacting the colonic air lumen.
- Tagging is homogeneous, i.e., the CT density values within the fluid pool are almost constant.

Based on the above EC assumptions, the majority of the existing EC methods are designed to mitigate PV effect, which causes unexpected ST-like layers at air-TM interfaces as well as aliasing artifacts at ST-TM interfaces after EC. These EC methods developed in the early stage are mainly categorized into two groups,



statistical and edge model-based methods.

The first group of EC methods employed the classifier of TMs based on statistical features [4, 30-32]. Chen et al. [30] classified each voxel by its local feature vector using a statistical model based on the Markov random field (MRF). They found the region boundary by dividing PV area into two subareas to mitigate the under or over estimation of region boundary due to the PV effect [see Figure 1.6]. Li et al. [31] reported an improvement by using a hidden MRF to integrate the neighborhood information for overcoming the inhomogeneity problems within the TMs.

Lately, Wang et al. [4] presented a PV segmentation method for the classification of each voxel that is composed of multiple materials by using the statistical expectation-maximization (EM) algorithm. Based on the assumption that observed CT density values follow a mixture of Gaussian distribution, the PV segmentation aimed to determine the Gaussian mixture model parameters and the material fractions within each voxel [see Figure 1.7]. Under the constraint that each voxel has a maximum of two materials, a MAP-EM solution is provided as a closed-form, and after the iterative PV segmentation, cleansing the TMs is performed by a series of dilation and erosion operations as well as region growing strategies. Wang et al. [32] improved their EM-based method by using a maximum a posteriori EM algorithm which simultaneously estimates material fractions at each voxel and statistical model parameters for the material distribution.

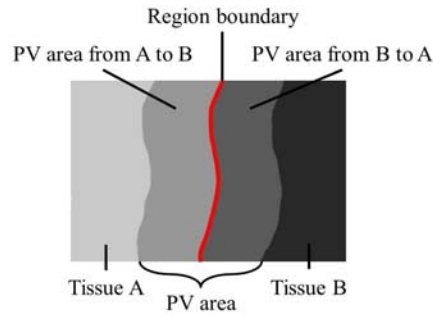


Figure 1.6 An example showing the intensity value change gradually from tissue A to tissue B. The red line represents the region boundary between tissue A and tissue B.

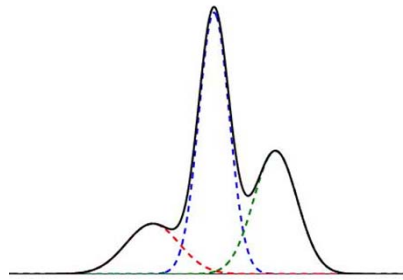


Figure 1.7 A mixture of Gaussian distribution. The *dotted lines (red, blue, and green)* represent three different Gaussian distributions with different means and variances for each tissue type. The *solid line (black)* shows a Gaussian mixture model representing an overall distribution of the observed CT density values.

Another group of EC methods used an edge model to delineate each type of transition between different materials [33-36]. Lakare et al. [33] analyzed the intensity profile along the ray to identify the boundary between two distinct regions [see Figure 1.8]. Once a ray detected a boundary between ST and TM based on its characteristic properties, the high intensity PV voxels at the ST-TM interface are removed and reconstructed by applying a smooth transfer function.

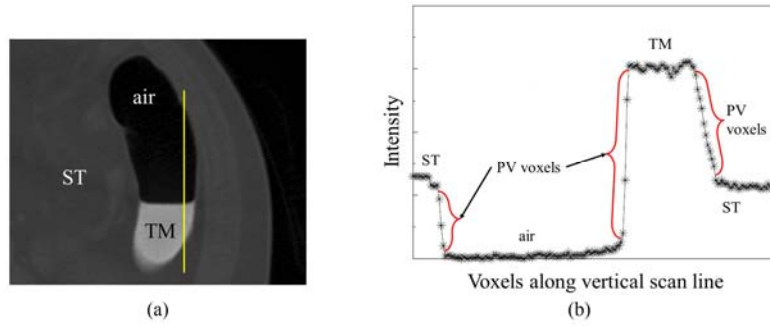


Figure 1.8 Example of a segmentation ray. (a) Part of a colon as seen from a traverse slice. (b) Intensity profile along the vertical scan line (yellow line in (a)).

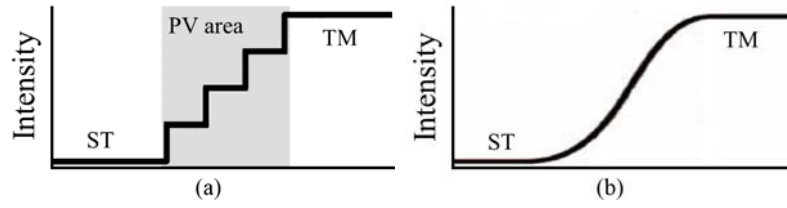


Figure 1.9 Mucosal reconstruction. (a) The stair-step scaffolding. (b) The smoothed stair-step scaffolding generated by applying a Gaussian low-pass filter.

Zalis et al. [34] used a combination of morphological and spatial filtering techniques to mitigate the volume averaging artifacts that occur near the boundary of TMs. They segmented the air-TM interfaces by employing a combination of selective edge detection and subtraction mask dilation. And then, they performed a mucosal reconstruction routine to address the aliasing artifacts at ST-TM interfaces. In the mucosal reconstruction, the PV voxels at ST-TM interfaces were formed into a stair-step scaffolding and smoothed with a Gaussian low-pass filter [see Figure 1.9].

Serlie et al. [35] proposed a scale- and rotation-invariant two-material transition model that estimates material fractions with sub-voxel accuracy. They used the CT density values and their gradient magnitude to characterize the boundary between

two distinct regions. Serlie et al. [36] extended this model as a scale-invariant three-material transition model by using an anisotropic point-spread function and sampling near T-junction where air, ST, and TM simultaneously meet.

### **1.3.2 Current status of EC**

Clinical investigators recently started to employ the reduced- or non-cathartic bowel preparation in CTC that can offer patients a well-tolerated and safely performed bowel preparation while providing a sensitivity and specificity similar to that of full-cathartic preparation in CTC examination. However, the aforementioned EC assumptions for full-cathartic CTC do not sustain in the reduced- or non-cathartic CTC images. Thus, the early EC methods that were developed for the full-cathartic CTC remain severely limited in removing irregularly shaped, randomly distributed, inhomogeneously tagged, and semi-solid stool that is the typical fecal residue in non-cathartic CTC, and they tend to generate severe cleansing artifacts that impair the diagnostic utility of the electronically cleansed CTC images [see Figure 1.10].

- State and homogeneity: Non-cathartic CTC has different states of TMs, including those in solid, semi-solid, and liquid state, whereas full-cathartic CTC has only liquid state TMs. Generally, contrast agents such as iodine are mixed more uniformly in liquid state than in solid state TMs; thus, non-cathartic CTC presents more inhomogeneously TMs than does full-cathartic CTC.
- Shape and size: Due to the flexibility of fluid, the TM in full-cathartic CTC

tends to appear as a bowl-shaped fluid pool at the bottom of a colonic lumen. In contrast, the shape of solid or semi-solid state TMs in non-cathartic CTC tends to be irregular. In addition, the size of the TM varies substantially.

- **Distribution:** The liquid state TM tends to be located at the bottom of a colonic lumen due to the gravitational effect, whereas solid or semi-solid state TMs in non-cathartic CTC may be distributed anywhere on the colonic wall, even at the ceiling of the colonic lumen against gravity, because of the relatively dry and thus viscous characteristics of the mucosal surface of the colonic wall.

Recent EC research has been focusing on the non-cathartic CTC studies. Cai et al. presented a structure-analysis EC method, which employed Hessian response field to enhance the submerged folds and polyps while other ST structures were de-enhanced, and local roughness field to distinguish thin ST layer from air-tagging boundaries. It effectively avoids the cleansing artifacts including soft-tissue degradation and pseudo-soft-tissue structures, which is generated in reduced- or non-cathartic CTC [38]. Recently, Cai et al. improved their method for obviating

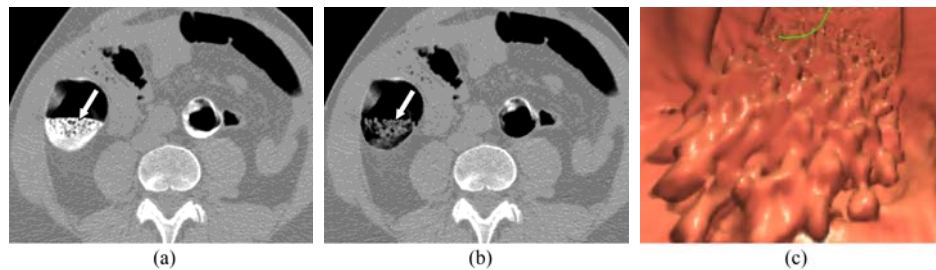


Figure 1.10 Incomplete cleansing. (a) CTC image shows a region of inhomogeneous stool (*arrow*). (b) CTC image shows incomplete cleansing of the stool, leaving heterogeneous material (*arrow*). (c) Three-dimensional endoluminal view image shows the incompletely cleansed fecal material. *Green line* indicates a portion of the colon centerline.

the incomplete cleansing artifacts in non-cathartic CTC, which is caused by the partial removal of only the TMs with high CT attenuation and leaving low-attenuation TMs uncleansed. They developed a mosaic decomposition EC method that decomposed the TMs into a set of local homogeneous subregions by application of a 3D watershed transform and a single-class support vector machine classifier to discriminate ST subregions from those of other materials [39].

## 1.4 Thesis contributions

First, we propose an EC method using a ST-preserving reconstruction model for removing TMs in CT images. To simultaneously mitigate PV and PEH effects, we integrate material fractions and structural responses into a single reconstruction model. In our approach, colonic components including air, TM, air-TM interface, and ST-TM interface are first segmented. For each voxel in the segmented TM and air-TM interface, CT density value is replaced with the pure material density of air and thus the unexpected ST-like layers at the air-TM interface (caused by PV effect) are simply removed. On the other hand, for each voxel in the segmented ST-TM interface, the two-material fractions of ST and TM are derived using a two-material transition model [35] and the structural response is calculated by the rut-enhancement function based on the eigenvalue signatures of the Hessian matrix [38]. Then, CT density value of each voxel in ST-TM interface is reconstructed based on both the material fractions and structural responses to conserve the PV contributions of ST in the voxel and preserve the folds and polyps submerged in TMs. Therefore, in our ST-preserving reconstruction model, the material fractions

remove the aliasing artifacts at the ST-TM interface (caused by PV effect) effectively while the structural responses avoid the erroneous cleansing of the submerged folds and polyps (caused by PEH effect).

Second, to remove the ridge-shaped artifacts at T-junctions where the interface layer between air and TM touches the colon wall, we propose a simplified three-material model. In addition to air, TM, air-TM interface, and ST-TM interface, T-junction is also segmented. For each voxel in the segmented T-junction, the three-material fractions of air, ST, and TM are derived using a three-material transition model. Although Serlie et al. [36] presented the three-material transition model, their method suffers from the high computational complexity of solving the orthogonal projection problem, in which the model representation with the minimum Euclidean distance to the observed measurements is found. To reduce the computational complexity, they generated a “code-book” of traces by uniformly sampling the model representation in material fraction space and found the best match between the observed measurements and the entries in the code-book. On the other hand, in this paper, we currently propose a simplified three-material model that provides a very quick estimate of the three-material fractions without the use of code-book. In our simplified three-material model, three pairs of two-material fractions are calculated by using the two-material transition model and then simply combined into a single triple of three-material fractions based on the barycentric interpolation in material fraction space. Using the three-material fractions, CT density values of voxels in T-junction are updated based on our ST-preserving reconstruction model, in the same manner as the voxels in ST-TM interface.

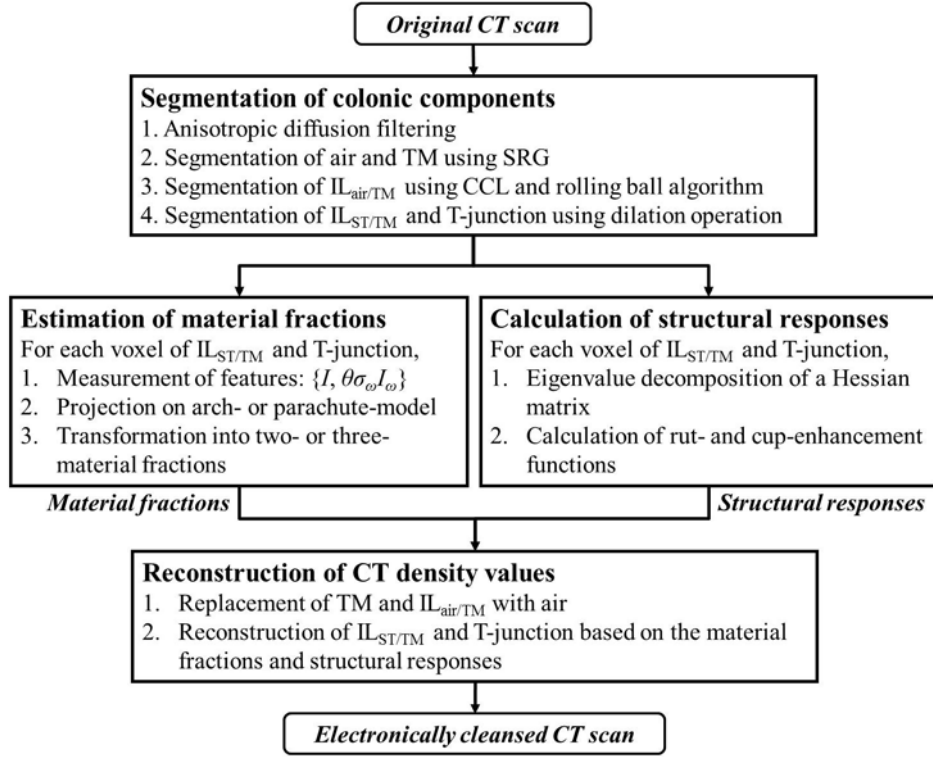


Figure 1.11 Process of the proposed EC method.

The proposed EC method consists of the following four major steps, as illustrated in Figure 1.11.

## 1.4 Thesis outline

The organization of the dissertation is as follows. Chapter 2 describes the segmentation of colonic components including air, TM, air-TM interface, ST-TM interface, and T-junction. Chapter 3 describes the estimation of material fractions. Two-material fractions of voxels in ST-TM interface are derived based on the two-



material model, whereas three-material fractions of the voxels in T-junction are estimated based on the three-material model, which is accelerated by using our new projection method. Chapter 4 explains structural response, which is used for detecting the folds and polyps submerged in TMs. Chapter 5 presents material fraction-based reconstruction model and ST-preserving reconstruction model. Chapter 6 presents the experimental results of the proposed EC method to clinical datasets. Finally, Chapter 6 summarizes and concludes this thesis.

## Chapter 2. Colon Segmentation

### 2.1 Overview

The anisotropic diffusion filtering is first applied, and then the colonic components including air, TM, air-TM interface layer ( $IL_{air/TM}$ ), ST-TM interface layer ( $IL_{ST/TM}$ ), and T-junction are segmented by the successive application of 3D seeded region growing (SRG), 3D connected component labeling (CCL), rolling ball algorithm, and dilation operation.

### 2.2 Anisotropic diffusion filter

First, each CT slice is pre-processed with an anisotropic diffusion filter [40] to smoothen contiguous regions (i.e., air and TM) while preserving the edge boundaries (i.e.,  $IL_{air/TM}$ ,  $IL_{ST/TM}$ , and T-junction) that occur between these regions.

Based on the scale-space technique, an image is represented as a family of smoothed images  $I(x, y; t)$ , which are obtained by convolving the original image

$I_0(x, y)$  with a Gaussian kernel  $G(x, y; t)$  of variance  $t$

$$I(x, y; t) = I_0(x, y) * G(x, y; t). \quad (2.1)$$

The parameter  $t$  in this family is referred to as the scale parameter and larger values

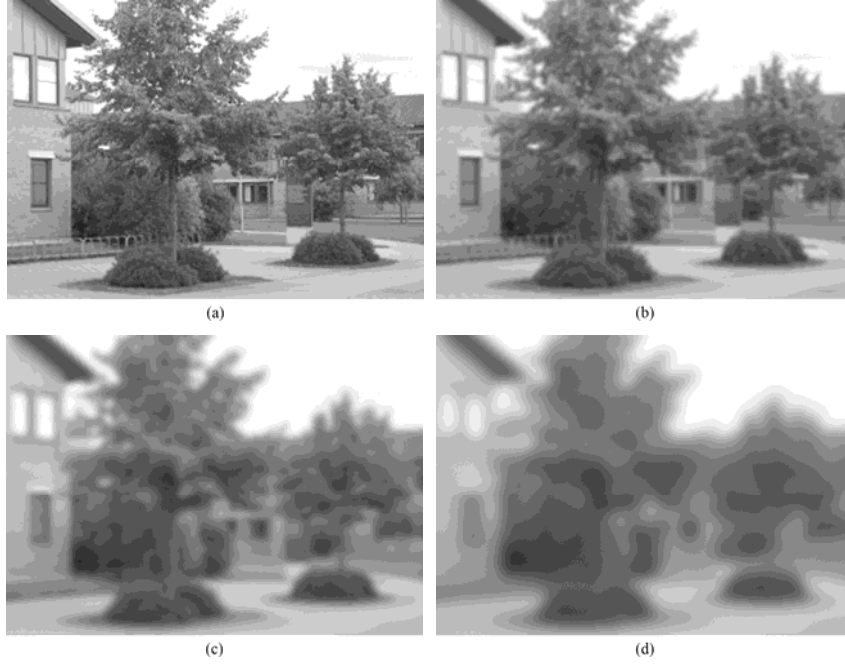


Figure 2.1 Example of the scale-space representation. (a)  $I(x, y; 0)$  at scale  $t = 0$ , corresponding to the original image  $I_0(x, y)$ . (b)-(d)  $I(x, y; t)$  at scale  $t = 1$ ,  $t = 4$ , and  $t = 16$ .

of  $t$  correspond to images at coarser resolutions [see Figure 2.1].

The one parameter family of smoothed images may equivalently be viewed as the solution of the isotropic diffusion equation

$$\frac{\partial I(x, y; t)}{\partial t} = \text{div}(\nabla I) \quad (2.2)$$

with the initial condition  $I(x, y; 0) = I_0(x, y)$ , where  $I_0(x, y)$  is the original image and  $\nabla I$  is the image gradient. Modifying the image according to this isotropic diffusion equation is equivalent to filtering the image with a Gaussian filter.

Perona and Malik [40] replaced the classical isotropic diffusion equation with

$$\frac{\partial I(x, y; t)}{\partial t} = \text{div} \left[ g(\|\nabla I\|) \nabla I \right] \quad (2.3)$$

where  $\|\nabla I\|$  is the gradient magnitude and  $g(\|\nabla I\|)$  is an “edge-stopping” function. This function is chose to satisfy  $g(x) \rightarrow 0$  when  $x \rightarrow \infty$  so that the diffusion is “stepped” across edges, resulting in the preservation of boundaries between the piecewise smooth regions in an image.

### 2.3 Segmentation of air and TM

To segment both air and TM simultaneously, we apply 3D SRG using separate thresholds for air and TM regions [37]. 3D SRG is initiated from one automatically placed seed point inside the air-filled lumen focusing on the cecum and rectum [41]. Given the seed point, each step of SRG incorporates one additional voxel into the region with similar property and the SRG procedure is repeated until there are no further changes in the evolving segmented region. To determine the similarity between the current voxel  $x$  and the intersected regions (i.e., air and TM), three criteria are used.

- 1) Absolute CT density values for air ( $T_{air}$ ) and TM ( $T_{TM}$ ): Voxels with densities lower than  $T_{air}$  are segmented as air and voxels with densities higher than  $T_{TM}$  are segmented as TM.
- 2) Difference ( $T_{diff}$ ) of density value with the mean densities of air and TM regions: Voxels that satisfy the condition  $\left| I(x) - \text{mean}_{y \in R_{air}} [I(y)] \right| \leq T_{diff}$

are segmented as air and voxels that satisfy the condition

$$\left| I(x) - \text{mean}_{y \in R_{TM}} [I(y)] \right| \leq T_{diff} \text{ are segmented as TM.}$$

- 3) Gradient magnitude ( $T_{grad}$ ) for edge detection: Voxels with a gradient magnitude greater than  $T_{grad}$  are considered as edges. In other words, voxels that satisfy the condition  $\|\nabla I(x)\| > T_{grad}$  are not segmented as air and TMs.

In this paper, the thresholds  $T_{air}$  and  $T_{TM}$  were experimentally set as -700 Hounsfield unit (HU) and 600 HU, respectively. And the thresholds  $T_{diff}$  and  $T_{grad}$  were set as 250 and 500.

Due to the PV effect, there is a thin ST-like layer between air and TM (i.e.,  $IL_{air/TM}$ ), in which density values of voxels are higher than  $T_{air}$  and lower than  $T_{TM}$ , so 3D SRG cannot proceed between air and TM across the  $IL_{air/TM}$ . To address this problem, a leaping is allowed from air to TM and vice versa during 3D SRG. A leaping occurs when one voxel in air and the other voxel in TM have the same x- and z- coordinates and their y-coordinates are different from each other by at most 5 voxels, which were experimentally determined. In addition, air voxel should be located above TM voxel due to the gravity effect.

## 2.4 Segmentation of air-TM interface

Because  $IL_{air/TM}$  is a flat surface between air and TM, the  $IL_{air/TM}$  is found by sending a ray from an air voxel and examining whether the ray reaches a TM voxel

within 5 voxels. A straight line in a direction of y-axis that connects two corresponding voxels is generated and voxels on the line are assigned to be  $IL_{air/TM}$ .

Considering that surface tension forces cause the meniscus effect, we refine the either end of  $IL_{air/TM}$  using rolling ball algorithm. First, the spatial relationships between the segmented air and TM need to be determined. All segmented regions are uniquely labeled using 3D CCL [42, 43], and then pairs of air and TM, which are connected to each other via  $IL_{air/TM}$ , are identified. For each pair of connected air and TM on each slice, the rolling ball algorithm with the radius of 7 voxels is applied [see Figure 2.2] [44]. A ball filter is successively placed tangential to each contour point of the connected air and TM, and then an indentation is identified when the boundary of the ball filter contacts the contour at more than one point. At T-junctions, where  $IL_{air/TM}$  meets with the colon wall, the boundary of the ball filter touches two distinct points that respectively belong to the air and TM contours. As a straight line that connects these two points is drawn to bridge the indentation, a new colon lumen contour are constructed and the voxels newly encompassed by

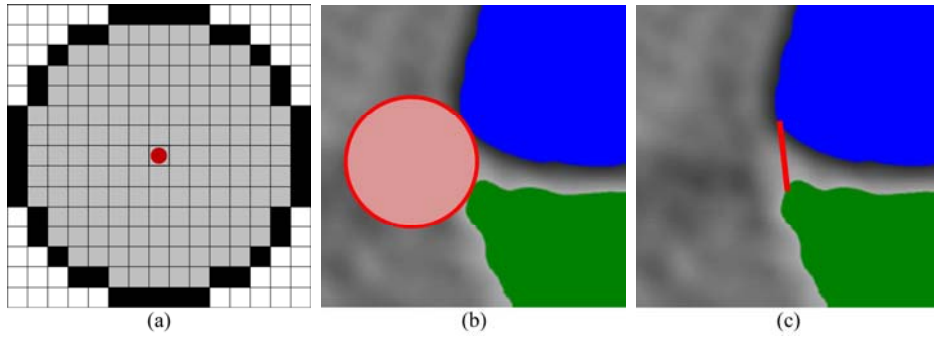


Figure 2.2 Rolling ball algorithm. (a) Ball filter with the radius of 7 voxels. (b) Magnified images at T-junction. Boundary of the ball filter touches two distinct points that respectively belong to the air (*blue*) and TM (*green*) contours. (c) Magnified images for indentation (*red*) that connects these two points.

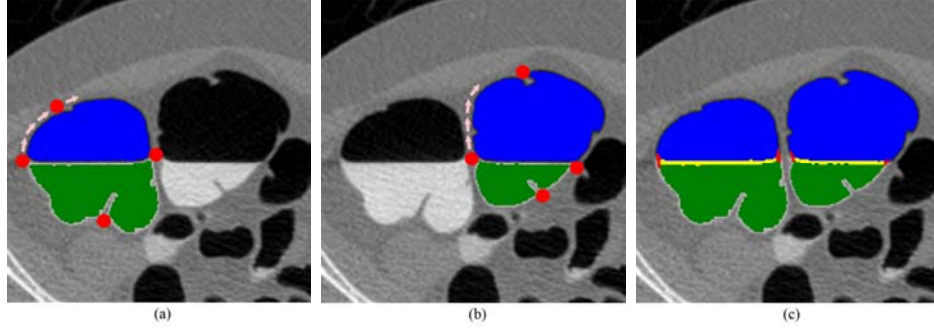


Figure 2.3 Segmentation of  $IL_{air/TM}$ . (a), (b) Magnified images for each pair of connected air (*blue*) and TM (*green*). The ball filter (*red circle*) is placed tangential to each contour point of the regions. (d) Magnified images of segmented  $IL_{air/TM}$  (*yellow and red*) between air and TM.

the final contour are additionally assigned to be  $IL_{air/TM}$  [see Figure 2.3].

## 2.5 Segmentation of ST-TM interface and T-junction

Finally, to segment  $IL_{ST/TM}$  and T-junction, the binary dilation operation is applied to the TM and  $IL_{air/TM}$ , respectively. Each TM is expanded with a  $3 \times 3 \times 3$  structuring element such that the newly expanded voxels are assigned to  $IL_{ST/TM}$  only when the newly expanded voxel was not included in any of air, TM, and  $IL_{air/TM}$ . In the same manner, the either end of  $IL_{air/TM}$ , where  $IL_{air/TM}$  touches the colon wall, is expanded and the expanded voxels are assigned to be T-junction.

## Chapter 3. Material Fraction Estimation

### 3.1 Overview

After segmentation of colonic components, each voxel in the colonic region is masked by one of five type components including air, TM,  $IL_{air/TM}$ ,  $IL_{ST/TM}$ , and T-junction. Each voxel in the air or TM is filled by a single material, whereas each voxel in  $IL_{air/TM}$ ,  $IL_{ST/TM}$ , or T-junction is composed of two or three different materials. Considering that TM would be eventually replaced with air,  $IL_{air/TM}$  involving the transition between air and TM should also be replaced with air regardless of material fractions of air and TM at each voxel. Therefore, for each voxel in air, TM, and  $IL_{air/TM}$ , the estimation of the material fractions is unnecessary. On the other hand, for each voxel in  $IL_{ST/TM}$  and T-junction, the CT density value needs to be reconstructed based on the material fractions to reduce the aliasing artifacts due to the PV effect. To derive the two- and three-material fractions at each voxel in  $IL_{ST/TM}$  and T-junction, we use the two-material transition model [35] and the “simplified” three-material model, respectively.

### 3.2 Two-material model

#### 3.2.1 Edge transition model



Based on the assumption that two materials (i.e., ST and TM) affect the density values of voxels in  $\Pi_{\text{ST/TM}}$ , a CT density value is modeled as a linear combination of pure material densities of ST and TM with corresponding material fractions

$$I = t_{ST} \cdot I_{ST} + t_{TM} \cdot I_{TM} . \quad (3.1)$$

where  $t_{ST} + t_{TM} = 1$ . Let  $I_{ST}$  and  $I_{TM}$  represent the pure material densities of ST and TM, respectively. And let  $t_{ST}$  and  $t_{TM}$  represent the corresponding material fractions of each material.

A transition between two materials is modeled by a unit-step function  $u(x)$  that is convolved with a Gaussian kernel  $g(x; \sigma)$  of standard deviation  $\sigma$  resulting in a cumulative Gaussian distribution

$$G(x; \sigma) = u(x) * g(x; \sigma) = \frac{1}{2} \left[ 1 + \operatorname{erf} \left( \frac{x}{\sigma \sqrt{2}} \right) \right] \quad (3.2)$$

with

$$u(x) = \begin{cases} 0 & x < 0 \\ 1 & x \geq 0 \end{cases} \quad (3.3)$$

$$g(x; \sigma) = \frac{1}{\sigma \sqrt{2\pi}} \exp \left( \frac{-x^2}{2\sigma^2} \right) \quad (3.4)$$

$$\operatorname{erf}(x) = \frac{2}{\sqrt{\pi}} \int_0^x \exp(-t^2) dt \quad (3.5)$$

This model deals with a two-material transition based on locally estimated derivative values, allowing slowly varying material densities at both sides of the transition. A compact description of edges is obtained using a gauge coordinate, a local Cartesian coordinate system with axes aligned to the intrinsic local image

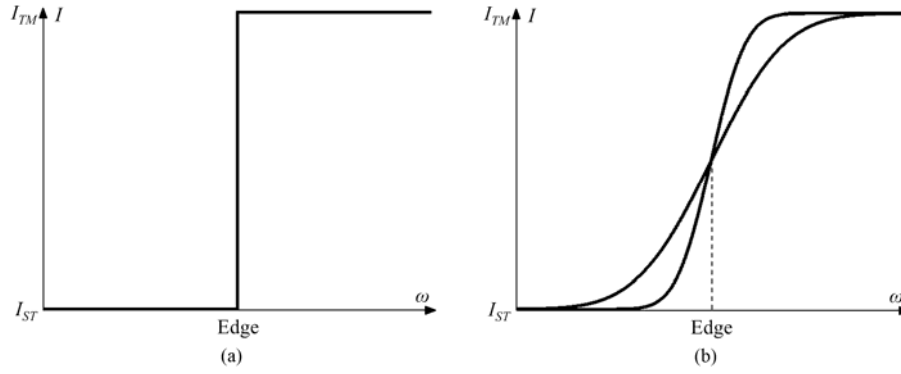


Figure 3.1 Two-material transition model. (a) Ideal two-material transition at  $IL_{ST/TM}$  modeled by the unit-step function. (b) Blurred two-material transition at  $IL_{ST/TM}$  modeled by the cumulative Gaussian distribution function.

coordinates. Let  $\omega$  represent the gradient direction and  $\sigma_\omega$  represent the scale of the Gaussian function along  $\omega$ . Notice that a description of transitions in gauge coordinates is by definition both rotation and translation invariant. The expected density values at opposite sides of the transition are  $I_{ST}$  and  $I_{TM}$  such that  $I(\omega; \sigma_\omega) \triangleq (I_{TM} - I_{ST})G(\omega; \sigma_\omega) + I_{ST}$  denotes the density value and  $I_\omega(\omega; \sigma_\omega) \triangleq (I_{TM} - I_{ST})g(\omega; \sigma_\omega)$  denotes the gradient magnitude (i.e., first derivative in gradient direction) [see Figure 3.1].

### 3.2.2 Arch model

The model presented here is inspired by the work of Kindlmann [45] and Kniss [46]. They plot the gradient magnitude  $I_\omega(\omega)$  as a function of density value

$I(\omega)$ . This yields arch-shaped point-clouds for edge regions [see Figure 3.2]. All arches, which connect the same two materials, share the same base along the horizontal axis, but have a height that is inversely proportional to  $\sigma_\omega$ . Consider the scale-invariant gradient magnitude  $\sigma_\omega I_\omega$  along a transition. Plotting  $(I, \sigma_\omega I_\omega)$  yields a single scale and rotation invariant arch that share the same height. The spread that remains is caused by noise [see Figure 3.2(b)].

An analytic expression for the scale-invariant arch function is derived as follows. First, we assume that the expected density values at the transition are 0 and 1 such that  $I(\omega; \sigma_\omega) \triangleq G(\omega; \sigma_\omega)$  denotes the density value and  $I_\omega(\omega; \sigma_\omega) \triangleq g(\omega; \sigma_\omega)$  denotes the gradient magnitude. And then, the inverse cumulative Gaussian function  $G^{-1}$  is obtained by inserting (3.2) in  $G(G^{-1}(x)) = x$  for  $x \in [0, 1]$ . Solving for  $G^{-1}(x)$  yields

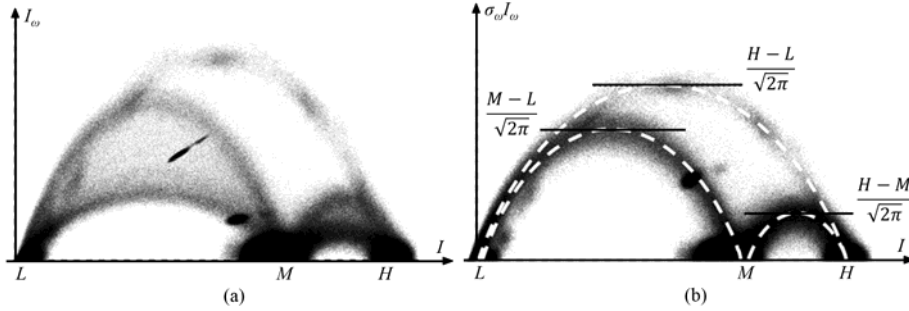


Figure 3.2 Arch-shaped point-clouds for edge regions. (a) Scatter plot of intensity and gradient magnitude. (b) Scatter plot of intensity and scale-invariant gradient magnitude. Three instantiations of the arch model are superimposed corresponding to the three types of material transitions.

$$\begin{aligned}
\frac{1}{2} \left[ 1 + \operatorname{erf} \left( \frac{G^{-1}(x; \sigma)}{\sigma \sqrt{2}} \right) \right] &= x \Leftrightarrow \\
\frac{G^{-1}(x; \sigma)}{\sigma \sqrt{2}} &= \operatorname{erf}^{-1}(2x - 1) \Leftrightarrow \quad . \quad (3.6) \\
G^{-1}(x; \sigma) &= \sigma \sqrt{2} \operatorname{erf}^{-1}(2x - 1)
\end{aligned}$$

The scale-invariant gradient magnitude is calculated by multiplying  $I_{\omega}(\omega; \sigma_{\omega}) \triangleq g(\omega; \sigma_{\omega})$  of (3.4) with  $\sigma_{\omega}$  and substituting  $x$  by  $G^{-1}(x)$  of (3.6). This yields

$$\begin{aligned}
\operatorname{arch}(x) &\triangleq \sigma g(G^{-1}(x; \sigma); \sigma) \\
&= \frac{1}{\sqrt{2\pi}} \exp \left( - \left\{ \operatorname{erf}^{-1}(2x - 1) \right\}^2 \right). \quad (3.7)
\end{aligned}$$

The arch function describes the scale-invariant gradient magnitude  $\sigma_{\omega} I_{\omega}$  as a function of density value  $I$  [see Figure 3.3].

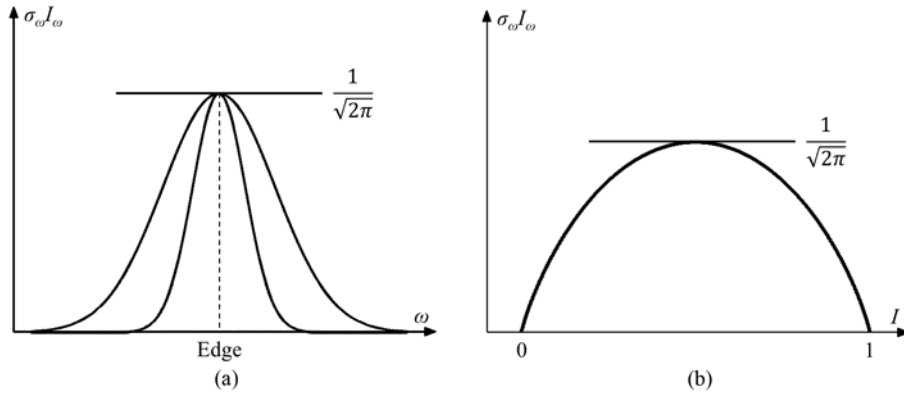


Figure 3.3 Scale-invariant arch. (a) Scale-invariant gradient magnitude as a function of position. (b) Scale-invariant gradient magnitude as a function of density value. Single arch is obtained upon plotting the scale-invariant gradient magnitude as a function of density value.

Finally, the description is now generalized by adding two parameters to represent the expected density values  $L$  and  $H$  with  $L < H$

$$\text{arch}(I; L, H) = (H - L) \text{arch}\left(\frac{I - L}{H - L}\right). \quad (3.8)$$

For each voxel in  $\text{IL}_{\text{ST/TM}}$ , the expected density values  $L$  and  $H$  correspond to  $I_{\text{ST}}$  and  $I_{\text{TM}}$ , respectively.

### 3.2.3 Noise isotropy

Measurements  $(I, \sigma_\omega I_\omega)$  yield the noise-free values contaminated by noise. The

noise is assumed to be Gaussian distributed with zero mean and variance  $\sigma_{ni}^2$  [47].

An estimate of these noise-free values is obtained by mapping the observed values

of  $(I, \sigma_\omega I_\omega)$  onto the closest point on the corresponding arch. The distance

metric to be used depends on the covariance matrix of the noise. The two

measurements are obtained by orthogonal operators. Hence, these measurements

have  $\text{cov}(I, \sigma_\omega I_\omega) = 0$ , but may display different variances. An isotropic

(Euclidean) metric can be used if the derivative is scaled by a factor  $\theta$  such that

the noise in  $(I, \theta \sigma_\omega I_\omega)$  is isotropic. In that case, we can use the orthogonal

projection from the point  $(I, \theta \sigma_\omega I_\omega)$  onto the  $\theta$ -weighted arch. The scale factor

$\theta$  was calculated based on the relation between the variance after anisotropic

Gaussian filtering and the variance of the noise when measuring the gradient

magnitude [48].

The relation between the variances of the noise before convolution  $\sigma_{ni}^2$  and after convolution  $\sigma_{no}^2$  with a  $n$ th-order Gaussian derivative of scale  $\sigma_{op}$  in  $D$ -dimensional space is [47]

$$\frac{\sigma_{no}^2}{\sigma_{ni}^2} = \frac{(2n)!}{\sigma_{op}^{D+2n} \pi^{D/2} n! 2^{D+2n}}. \quad (3.9)$$

Typically, for medical images, the sampling along the scanner's z-axis (axial, slice pitch, out-of-plane) is often lower when compared to the x- and y-axis (lateral or in-plane). We would like to use Gaussian derivative filters that are not sampled isotropically to minimize additional blurring. Let  $\Delta$  denote the sampling pitch of the signal. As a rule of thumb, the Gaussian operator should obey  $\sigma_{op} \geq 0.9\Delta$  to meet the Nyquist sampling criterion [49]. Using smaller scales requires interpolation of the data, which reduces  $\Delta$  to satisfy the sampling criterion. In three steps, we 1) compute the variance after anisotropic Gaussian filtering, 2) compute the variance of the gradient magnitude as a function of anisotropic Gaussian filtering and edge orientation, and 3) increase the gradient magnitude by a scale factor to make the noise isotropic.

First, consider the variance of the noise after  $0$ th-order Gaussian filtering: the first dimension of  $(I, \theta \sigma_{\omega} I_{\omega})$  and the independent variable of  $\text{arch}(x)$ . Let  $\sigma_{op,z}$  be the axial scale and  $\sigma_{op,\perp z}$  be the lateral scale of the operator with respect to the z-direction. Decomposition of the Gaussian filter into an axial and a

lateral component requires that we apply (3.9) with  $(\sigma_{op,z}, n=0, D=1)$  and

$(\sigma_{op,\perp z}, n=0, D=2)$ , respectively

$$\frac{\sigma_{no,z}^2}{\sigma_{ni}^2} = \frac{1}{\sigma_{op,z} 2\sqrt{\pi}}, \quad \frac{\sigma_{no,\perp z}^2}{\sigma_{ni}^2} = \frac{1}{\sigma_{op,\perp z}^2 4\pi}. \quad (3.10)$$

Given that the two convolutions are applied in series (in arbitrary order since the convolution operator is commutative),  $\sigma_{no}$  of the first pass is substituted for  $\sigma_{ni}$  of the second pass. This gives a fixed variance after filtering in 3D, irrespective of the orientation of the edge  $\omega$

$$\sigma_{no}^2 = \sigma_I^2 = \frac{\sigma_{ni}^2}{\sigma_{op,z} \sigma_{op,\perp z}^2 2^3 \pi^{3/2}}. \quad (3.11)$$

$\sigma_I^2$  represents the variance of the noise on  $I$  after filtering.

Second, consider the variance of the noise when measuring the gradient magnitude: the second dimension of  $(I, \theta \sigma_\omega I_\omega)$  and the result of  $\text{arch}(x)$ . This 3D operation can be decomposed into a 1D first Gaussian derivative filter in the gradient direction  $\omega$  and a 2D Gaussian filter in the plane perpendicular to  $\omega$ . Let  $\sigma_{op,\omega}$  be the effective scale of the operator in the gradient direction  $\omega$  as a function of the angle  $\alpha_\Delta$  between  $z$  and  $\omega$

$$\sigma_{op,\omega} = \sqrt{(\sin(\alpha_\Delta) \sigma_{op,\perp z})^2 + (\cos(\alpha_\Delta) \sigma_{op,z})^2}. \quad (3.12)$$

Applying (3.9) with  $(\sigma_{op,\omega}, n=1, D=1)$  and  $(\sigma_{op,\perp\omega}, n=0, D=2)$ ,

respectively, gives

$$\frac{\sigma_{no,\omega}^2}{\sigma_{ni}^2} = \frac{1}{\sigma_{op,\omega}^3 4\sqrt{\pi}}, \quad \frac{\sigma_{no,\perp\omega}^2}{\sigma_{ni}^2} = \frac{1}{\sigma_{op,\perp\omega}^2 4\pi}. \quad (3.13)$$

These two convolutions applied in series provide the variance of the noise after filtering in 3D

$$\sigma_{no}^2 = \sigma_{I_\omega}^2 = \frac{\sigma_{ni}^2}{\sigma_{op,\omega}^3 \sigma_{op,\perp\omega}^2 2^4 \pi^{3/2}}. \quad (3.14)$$

Note that the variance of the gradient-magnitude remains a function of the edge orientation  $\omega$ . Finally, using (3.11) and (3.14), the noise in  $(I, \theta \sigma_\omega I_\omega)$  is made isotropic with

$$\theta = \frac{1}{\sigma_\omega} \cdot \frac{\sigma_I}{\sigma_{I_\omega}} = \frac{1}{\sigma_\omega} \cdot \frac{\sigma_{op,\omega}^{3/2} \sigma_{op,\perp\omega} \sqrt{2}}{\sqrt{\sigma_{op,z} \sigma_{op,\perp z}}}. \quad (3.15)$$

Suppose, for example, that a Gaussian operator isotropic in  $\Delta$  is used to measure derivatives with  $\sigma_{op,z} = \sigma_{op,\perp z} = \sigma_{op,\omega} = \sigma_{op,\perp\omega}$ . Then (3.15) is simplified considerably such that  $\theta = (\sigma_{op} \sqrt{2}) / \sigma_\omega$ .

### 3.2.4 Orthogonal projection on the arch

Considering that these measurements display different noise variances due to different samplings along x-, y-, and z-axis of the CT scanner, we scale them in



such a way as to obtain isotropic noise:  $(I, \theta \sigma_\omega I_\omega)$ . After that, we estimate the noise-free value using the orthogonal projection that maps the point  $(I, \theta \sigma_\omega I_\omega)$  onto the closest point  $(I', \theta \sigma_\omega I'_\omega)$  on the  $\theta$ -weighted arch. The relative position of the estimated density value  $I'$  between  $I_{ST}$  and  $I_{TM}$  yields the material fractions of ST and TM at the voxel in  $\Pi_{ST/TM}$ . With  $(I', \theta \sigma_\omega I'_\omega)$  the orthogonal projection of the point  $(I, \theta \sigma_\omega I_\omega)$  onto the selected arch,  $t_{ST}$  and  $t_{TM}$  represent the material fractions corresponding to ST and TM, respectively. These material fractions are obtained by [see Figure 3.4]

$$t_{ST} = \frac{I_{TM} - I'}{I_{TM} - I_{ST}}, \quad t_{TM} = \frac{I' - I_{ST}}{I_{TM} - I_{ST}} = 1 - t_{ST}. \quad (3.16)$$

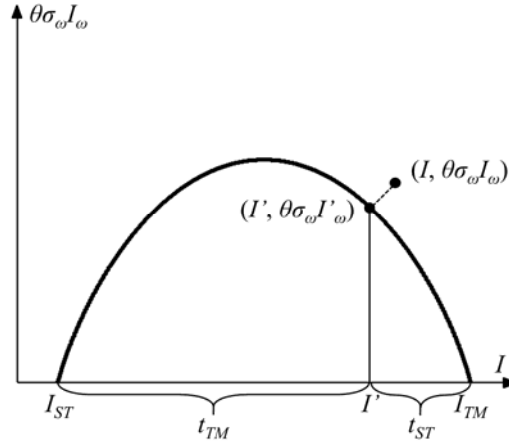


Figure 3.4 Estimation of material fractions of ST and TM using orthogonal projection on the arch.

### 3.3 Three-material model

#### 3.3.1 Junction transition model

A CT density value in T-junction is modeled as a linear combination of pure material densities of air, ST, and TM with corresponding material fractions

$$I = t_{air} \cdot I_{air} + t_{ST} \cdot I_{ST} + t_{TM} \cdot I_{TM} . \quad (3.17)$$

where  $t_{air} + t_{ST} + t_{TM} = 1$ . Let  $I_{air}$ ,  $I_{ST}$ , and  $I_{TM}$  represent the pure material densities of air, ST, and TM, respectively. And let  $t_{air}$ ,  $t_{ST}$ , and  $t_{TM}$  represent the corresponding material fractions of each material.

At T-junction, the IL<sub>air/TM</sub> meets the colon surface at a variety of angles to form a three-material transition [see Figure 3.5]. We will initially use a T-junction with  $\alpha = 90^\circ$  to illustrate our method. Other angles are analyzed by the same paradigm.

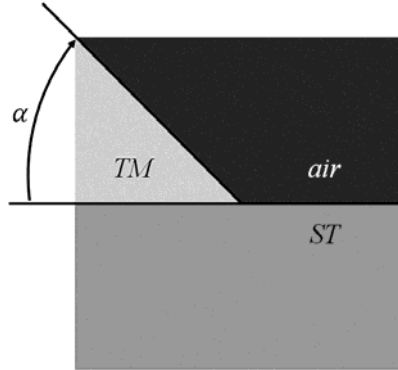


Figure 3.5 Configuration of three-material transition at a T-junction.

Let the junction model  $v$  be the intersection of three edges [see Figure 3.6(a)]

$$v(x, y, z) = \begin{cases} I_{air}, & x < 0, y < 0 \\ I_{ST}, & x \geq 0 \\ I_{TM}, & x < 0, y \geq 0 \end{cases} \quad (3.18)$$

$$= I_{air} + (I_{TM} - I_{air})u(-x)u(y) + (I_{ST} - I_{air})u(x)$$

Let  $V$  represent the junction model after convolution with a 3D Gaussian [see Figure 3.6(b)]. We assume that  $\sigma_x$ ,  $\sigma_y$ , and  $\sigma_z$  denote, respectively, the effective scale of the Gaussian operators in x-, y-, and z-directions

$$V(x, y, z) = I_{air} + (I_{TM} - I_{air})G(-x; \sigma_x)G(y; \sigma_y) + (I_{ST} - I_{air})G(x; \sigma_x) \quad (3.19)$$

$V_\omega$  describes the gradient magnitude at the junction [see Figure 3.6(c)]

$$V_\omega(x, y, z) \triangleq \|\nabla V(x, y, z)\| \quad (3.20)$$

with

$$\nabla V(x, y, z) = \begin{bmatrix} -(I_{TM} - I_{air})g(-x; \sigma_x)G(y; \sigma_y) + (I_{ST} - I_{air})g(x; \sigma_x) \\ (I_{TM} - I_{air})g(y; \sigma_y)G(-x; \sigma_x) \\ 0 \end{bmatrix} \quad (3.21)$$

In the same manner as in the two-material transition model, scaling the gradient magnitude by  $\sigma_\omega$  yields the scale-invariant gradient magnitude. This results in identical amplitudes of the gradient magnitude at the edge for measurements of different scales.

Let  $V_{\omega\omega}$  correspond to the second derivative in gradient direction of the junction model defined in (8) [see Figure 3.6(d)]. Due to the translation invariance along z

(i.e., the direction parallel to the fluid level in the junction model), we get

$$V_{\omega\omega}(x, y, z) = \frac{V_x^2 V_{xx} + V_y^2 V_{yy} + 2V_x V_y V_{xy}}{V_x^2 + V_y^2}. \quad (3.22)$$

Similarly to scaling of the first-order derivative, multiplication with  $\sigma_\omega^2$  yields the scale-invariant second derivative measured at the junction.

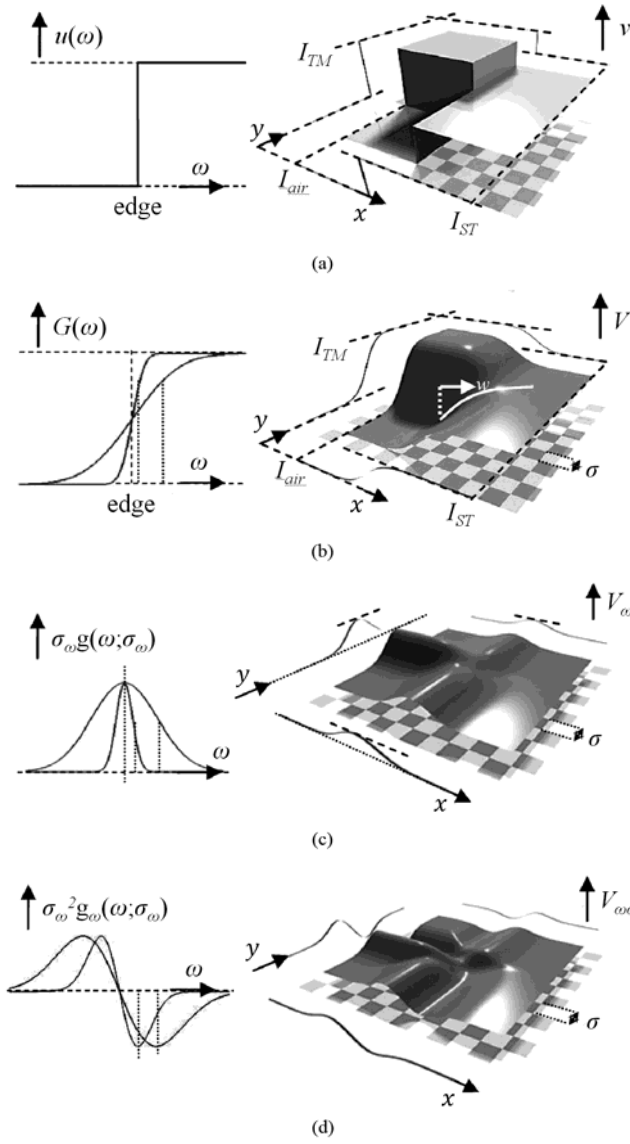


Figure 3.6 Three-material transition model with  $\alpha = 90^\circ$ . (a) Ideal three-material transition at T-junction modeled by the unit-step function. (b) Blurred three-material transition modeled by the cumulative Gaussian distribution function. (c) Gradient magnitude as a function of position. (d) Second directional derivative as a function of position.

### 3.3.2 Parachute model

The two-material transition model is extended into a three-material transition model by using a homogeneous barycentric coordinate on triangle. Each instance of three-material fractions  $(t_{air}, t_{ST}, t_{TM})$  corresponds to a barycentric point  $BP$  in a triangular domain  $(C_{air}, C_{ST}, C_{TM})$ , reflecting the proportion of the areas of the three sub-triangles defined by the  $BP$  and the two corners of the triangle. Considering the typical CTC images, most voxels are dominated by pure material (i.e., air, ST, and TM): the corners of the triangle. Fewer voxels participate in two-material transitions: the edges of the triangle. The smallest number of voxels participates in three-material transitions: the interior of the triangle [see Figure 3.7].

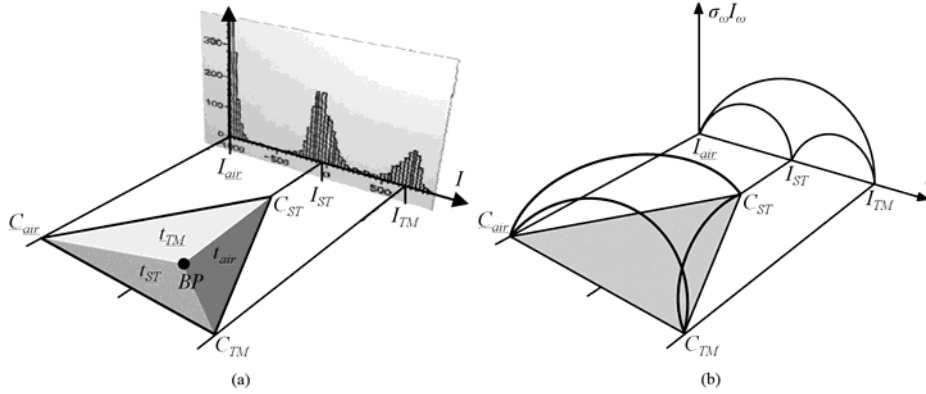


Figure 3.7 Barycentric coordinate in a triangular domain  $(C_{air}, C_{ST}, C_{TM})$ . (a) Image acquisition combines contributions of different materials into the partial volume CT density value. These contributions are represented as barycentric positions  $(t_{air}, t_{ST}, t_{TM})$ .  $I_{air}$ ,  $I_{ST}$ , and  $I_{TM}$  represent the expected CT density values of air, ST, and TM, respectively. (b) Edges of the triangle denote mixtures of two materials, corresponding to the arches for two-material transition.

In three-material transition model, the first derivatives of CT density value (in material fraction space as a barycentric coordinate and not in image space) are modeled by the first-order parachute function [see Figure 3.8(a)]. The function is named “*parachute*,” because the surface created by the gradient magnitude as a function of material fractions reminds us of a parachute.

We derive an analytical expression of the function to map material fractions onto a position in image space  $(x, y)$ , in which, subsequently, the derivatives are computed. First, notice that  $t_{ST}$  does not depend on  $y$  (3.19). Consequently, the inverse cumulative Gaussian relates  $x$  to  $t_{ST}$

$$x = G^{-1}(t_{ST}; \sigma_x). \quad (3.23)$$

The inverse cumulative Gaussian function  $G^{-1}$  is obtained by inserting (3.2) in  $G(G^{-1}(x)) = x$  as explained in two-material model. Solving for  $G^{-1}(x)$  yields

$$G^{-1}(x; \sigma) = \sigma \sqrt{2} \operatorname{erf}^{-1}(2x - 1), \quad x \in [0, 1]. \quad (3.24)$$

Second,  $t_{TM}$  is regarded. Considering that

$$t_{TM} = G(-x; \sigma_x) G(y; \sigma_y) \quad (3.25)$$

and

$$t_{ST} = G(x; \sigma_x) \Leftrightarrow 1 - t_{ST} = G(-x; \sigma_x), \quad (3.26)$$

(3.25) is rewritten into

$$t_{TM} = (1 - t_{ST}) G(y; \sigma_y) \Leftrightarrow G(y; \sigma_y) = \frac{t_{TM}}{1 - t_{ST}} \quad (3.27)$$

from which we derive

$$y = G^{-1}\left(\frac{t_{TM}}{1-t_{ST}}; \sigma_y\right). \quad (3.28)$$

Third, the generalized parachute function describes the scale invariant  $n$ th-order derivative along the gradient direction as a function of material fraction by inserting (3.23) and (3.28) in either (3.19), (3.20), or (3.22), respectively, for  $n = 0$ , 1, or 2

$$\begin{aligned} \text{parachute}^0(t_{air}, t_{ST}, t_{TM}) &= V(x, y, z) \\ \text{parachute}^1(t_{air}, t_{ST}, t_{TM}) &= \sigma_\omega V_\omega(x, y, z) \\ \text{parachute}^2(t_{air}, t_{ST}, t_{TM}) &= \sigma_\omega^2 V_{\omega\omega}(x, y, z) \end{aligned} \quad (3.29)$$

with  $x$  and  $y$  functions of the material fractions as presented by (3.23) and (3.28). Note that the orientation of the T-junction was chosen in such a way that all  $z$ -dependencies have vanished. Analogous to (3.29), higher order derivatives may be computed as well. Figure 3.8(a) illustrates the first-order parachute function, showing  $V_\omega$  as a function of barycentric coordinates  $(1-t_{ST}-t_{TM}, t_{ST}, t_{TM})$ .

Properties of the first-order parachute function are as follows.

- 1) Corners of the triangle denote pure materials with all partial derivatives equal to zero.
- 2) Edges of the triangle denote mixtures of two materials with the scale-invariant gradient magnitude being given by the arch function [35].
- 3) Interior of the triangle denotes mixtures of three materials.
- 4) The parachute model is scale invariant at the underlying transitions due to the use of scale-invariant derivatives.



### 3.3.3 Noise isotropy

The measurement triplet  $(I, \sigma_\omega I_\omega, \sigma_\omega^2 I_{\omega\omega})$  is obtained by Gaussian derivative operators and display different noise variances. An approximation of the noise-free signal values will be obtained by finding the closest point on a model. A Euclidean metric can be used to do so only if the noise on the features is isotropic, which is imposed by scaling the derivatives:  $(I, \theta_1 \sigma_\omega I_\omega, \theta_2 \sigma_\omega^2 I_{\omega\omega})$ .

The ratio of a signal's noise variance of before convolution  $\sigma_{ni}^2$  and after convolution  $\sigma_{no}^2$  with a  $n$ th-order Gaussian derivative of scale  $\sigma_{op}$  in  $D$ -dimensional space is [47]

$$\frac{\sigma_{no}^2}{\sigma_{ni}^2} = \frac{(2n)!}{\sigma_{op}^{D+2n} \pi^{D/2} n! 2^{D+2n}}. \quad (3.30)$$

This result is used to predict the variances of noise in  $(I, \sigma_\omega I_\omega, \sigma_\omega^2 I_{\omega\omega})$  and to compensate for the differences. The scaling of the first axis is taken unaltered (i.e.,  $\theta_0 = 1$ ).

An elaborate deduction of the scaling parameter  $\theta_1$  for the first derivative was described previously in two-material model. Its calculation is initiated by determining the relative variance of the noise on  $I$  due to the anisotropic Gaussian filtering:  $\sigma_I^2 / \sigma_{ni}^2$  (in which  $\sigma_{ni}^2$  is now the hypothetical noise variance prior to filtering). Typically, the sampling along the scanner's z-axis is

lower when compared to the x- and y-axis. Let  $\sigma_{op,z}$  be the axial scale and  $\sigma_{op,\perp z}$  be the lateral scale of the operator with respect to the z-direction. Effectively, it is decomposed into an axial and a lateral component after which a concatenated application of (3.30) with  $(\sigma_{op,z}, n=0, D=1)$  and  $(\sigma_{op,\perp z}, n=0, D=2)$ , resulting in  $\sigma_I^2/\sigma_{ni}^2$  as (3.11).

The relative variance of the noise on  $I_\omega$ ,  $\sigma_{I_\omega}^2/\sigma_{ni}^2$  is calculated in a similar way. Let  $\sigma_{op,\omega}$  represent the effective scale of the Gaussian derivative filter in the gradient direction  $\omega$  and  $\sigma_{op,\perp\omega}$  the lateral scale.  $\sigma_{I_\omega}^2/\sigma_{ni}^2$  is obtained as (3.14) via (3.30) using  $(\sigma_{op,\omega}, n=1, D=1)$  and  $(\sigma_{op,\perp\omega}, n=0, D=2)$ .

At last,  $\theta_1$  is given by

$$\theta_1 = \frac{1}{\sigma_\omega} \cdot \frac{\sigma_I}{\sigma_{I_\omega}} = \frac{1}{\sigma_\omega} \cdot \frac{\sigma_{op,\omega}^{3/2} \sigma_{op,\perp\omega} \sqrt{2}}{\sqrt{\sigma_{op,z} \sigma_{op,\perp z}}} \quad (3.31)$$

in which the factor  $1/\sigma_\omega$  is needed to compensate for the scaling in  $\sigma_\omega I_\omega$ .

Analogously, a second scaling parameter  $\theta_2$  for the second derivative may be calculated to be

$$\theta_2 = \frac{1}{\sigma_\omega^2} \cdot \frac{\sigma_I}{\sigma_{I_{\omega\omega}}} = \frac{1}{\sigma_\omega^2} \cdot \frac{\sigma_{op,\omega}^{3/2} \sigma_{op,\perp\omega} \sqrt{2}}{\sqrt{\sigma_{op,z} \sigma_{op,\perp z}}} \quad (3.32)$$

### 3.3.4 Orthogonal projection on the parachute

For each voxel at T-junction, the material fractions of three materials are estimated by determining  $BP$  in the interior of the triangle. However, the data measurement pair  $(I, \theta \sigma_\omega I_\omega)$ , which was sufficient information to estimate two-material fractions, leads to ambiguity in the estimation of three-material fractions because probing the surface of first-order parachute function along the given CT density value  $I$  results in the equal altitude for two different positions [see Figure 3.8(c)].

To resolve this ambiguity, the second derivative term should be included. Therefore, the data measurement triplet  $(I, \theta_1 \sigma_\omega I_\omega, \theta_2 \sigma_\omega^2 I_{\omega\omega})$  should be projected onto the first-order as well as second-order parachute functions [see Figures 3.8(b) and (d)].

The final projection point at the parachute functions that yields the minimum Euclidean distance to the data measurements  $(I, \theta_1 \sigma_\omega I_\omega, \theta_2 \sigma_\omega^2 I_{\omega\omega})$  is determined by minimizing the sum of square residuals as follows:

$$\begin{aligned} \mathbf{t} &= (t_{air}, t_{ST}, t_{TM})^T \\ &= \arg \min_{t_{air}, t_{ST}, t_{TM}} \sum_{n=0}^2 \theta_n^2 \left\| \sigma_\omega^n I^{(n)} - \text{parachute}^{(n)}(t_{air}, t_{ST}, t_{TM}) \right\|^2 \end{aligned} \quad (3.33)$$

where  $I^{(n)}$  is the  $n$ th Gaussian derivative in gradient direction and  $\text{parachute}^{(n)}(t_{air}, t_{ST}, t_{TM})$  is the  $n$ th-order parachute function.  $t_m$  represents the material fraction of material  $m$  at the point of the trajectory on the parachute function.  $\theta_n$  is the scale factor for the  $n$ th derivative to obtain isotropic noise in

the same manner as the two-material transition model.

However, this orthogonal projection of the data measurement triplet  $(I, \theta_1 \sigma_\omega I_\omega, \theta_2 \sigma_\omega^2 I_{\omega\omega})$  on the parachute function suffers from the high

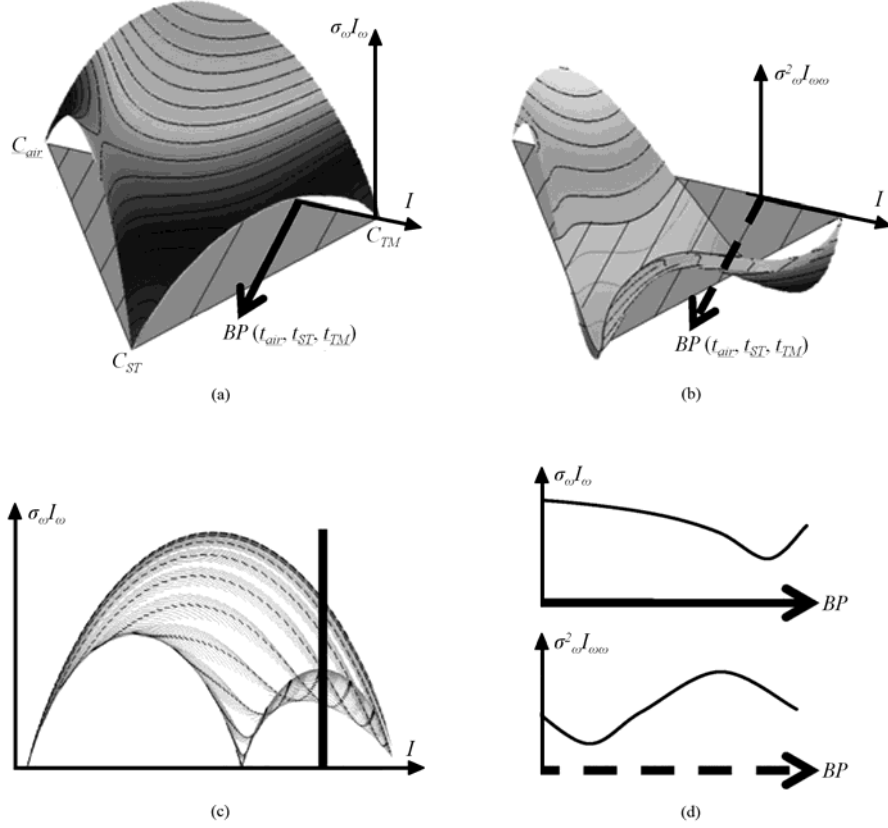


Figure 3.8 Parachute projection. (a) First-order parachute function displaying  $\sigma_\omega I_\omega$  as function of barycentric position. (b) Second-order parachute function displaying  $\sigma_\omega^2 I_{\omega\omega}$  as function of barycentric position. (c) Ambiguity in the estimation of three-material fractions using the data measurement pair  $(I, \theta \sigma_\omega I_\omega)$ . Probing the surface of the first-order parachute function along a fixed density (*dark line*) results in equal altitude for two positions. (d) Including the second derivative (b) in gradient direction (*dashed line*) solves this problem. This can be seen since equal gradient magnitudes have different second derivative in gradient direction.

computational complexity. To reduce the computational complexity of the orthogonal projection for three-material model, *Serlie et al.* [36] implemented the projection problem in a numerical manner. In the pre-processing step, they generated a “code-book” of traces by uniformly sampling the three-material model representation in material fraction space. And then, the optimal three-material fractions were approximately determined by finding the best match entry between the observed measurements and the entries in the code-book. That is, the use of the code-book leads to a reduced computational complexity by converting the orthogonal projection problem into a simple matching problem on a set of possible three-material fractions.

However, it still requires too much computation time compared to the orthogonal projection for the two-material model, because the observed measurements for every voxel in T-junction should be compared to all of the entries in the code-book. Besides, considering that the code-book is generated by uniformly sampling the model representation in material fraction space, the temporal resolution of the sampling limits the precision of the estimated three-material fractions [see Figure 3.9]. Thus, as the sampling rate decreases to establish a more accurate estimation, the growth of code-book makes the processing time for finding the best match entry increase critically. As a computationally more efficient alternative, in this paper, we currently propose a new projection method for the three-material model that provides a very quick estimate of the three-material fractions without the use of code-book.

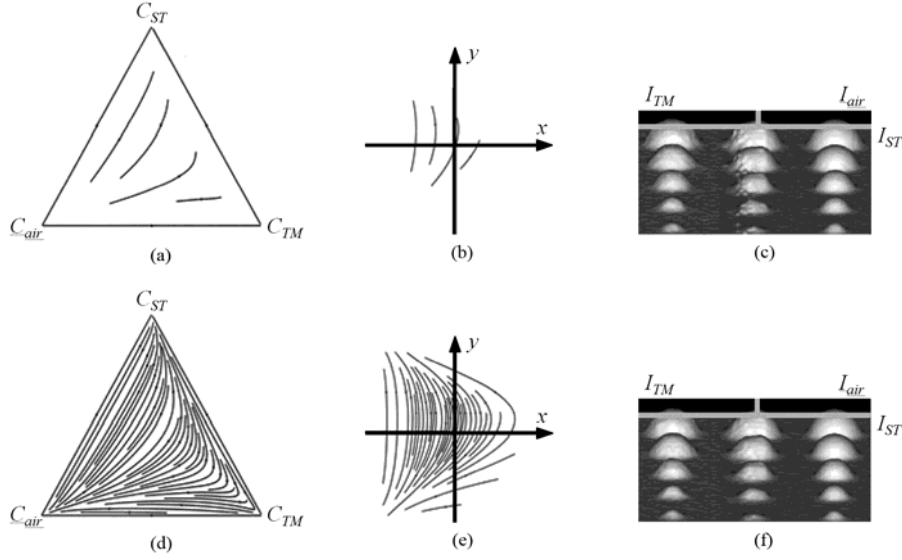


Figure 3.9 Sampling of model representation. (a), (d) Streamlines along  $\omega$  generated in barycentric space until the distance between the lines is below a certain minimum: 0.2 and 0.05 (distances in material fraction). (b), (e) Corresponding streamlines in image space. (c), (f) Artifacts from undersampling. Artificially generated polyps are used with sizes 3, 5, 7, 9, and 11 mm and  $\sigma = 1$  mm. The left part of middle polyps connects to TM and right part connects to air.

### 3.3.5 Fast projection based on the barycentric interpolation

To accelerate the estimation of the three-material fractions, we currently propose a new projection method for the three-material model. Without the use of code-book, the new projection method provides a very quick estimate of the three-material fractions by converting the orthogonal projection for the three-material model into that for the two-material model. Three pairs of two-material fractions are calculated by using the two-material model and then simply combined into a single triple of

three-material fractions based on the barycentric interpolation in material fraction space.

Since three materials (i.e., air, ST, and TM) affect the density values of voxels in T-junction, three different arch curves can be constructed to represent three kinds of two-material transitions (i.e., air-ST, air-TM, and ST-TM) in T-junction. These arches coincide with the edges of the triangle in a barycentric coordinate when the vertices of the triangle represent three pure materials. First, for each voxel, the data measurement pair  $(I, \theta \sigma_\omega I_\omega)$  is projected onto the closest points on three arch curves, which represent three kinds of two-material transitions. Then, the arch-projection points  $APs$  derive three pairs of two-material fractions at the voxel. In the barycentric coordinate associated with three materials (i.e., air, ST, and TM), each of three  $APs$  is located on each edge of the triangle [see Figure 3.10].

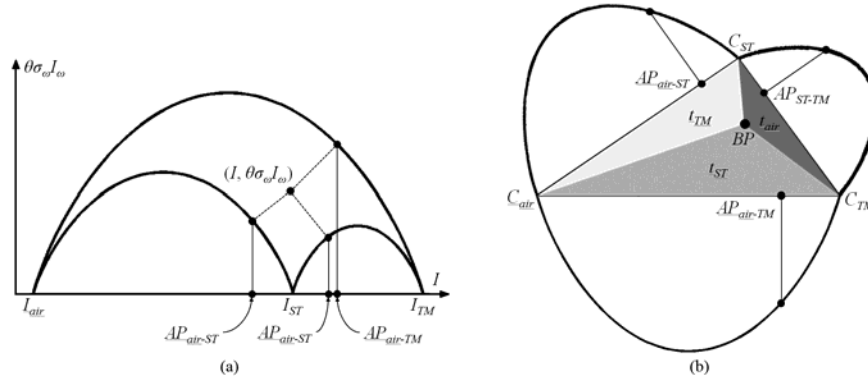


Figure 3.10 Proposed parachute projection method. (a) Three arch projections of data measurement pair  $(I, \theta \sigma_\omega I_\omega)$ . The positions of three arch-projection points  $APs$  derive three pairs of two-material fractions. (b) Barycentric interpolation in a triangular domain  $(C_{air}, C_{ST}, C_{TM})$ . When using uniform weights, barycentric point  $BP$  is determined as the center of the triangle formed by three  $APs$ . The proportion of the areas of three sub-triangles (*light grey*, *grey*, and *dark grey*) represents the three-material fractions.

$$\begin{aligned}
AP_{air-ST} &= t_{air/(air-ST)} \cdot C_{air} + t_{ST/(air-ST)} \cdot C_{ST} , \\
AP_{air-TM} &= t_{air/(air-TM)} \cdot C_{air} + t_{TM/(air-TM)} \cdot C_{TM} , \\
AP_{ST-TM} &= t_{ST/(ST-TM)} \cdot C_{ST} + t_{TM/(ST-TM)} \cdot C_{TM}
\end{aligned} \tag{3.34}$$

where  $t_{A/(A-B)}$  represents the material fraction of  $A$  between two-materials  $A$  and  $B$ ,

therefore, the following equations are derived

$$\begin{aligned}
t_{air/(air-ST)} + t_{ST/(air-ST)} &= t_{air/(air-TM)} + t_{TM/(air-TM)} \\
&= t_{ST/(ST-TM)} + t_{TM/(ST-TM)} = 1 .
\end{aligned} \tag{3.35}$$

Finally, the barycentric interpolation of three  $AP$ s generates a single  $BP$  in the interior of the triangle as follows:

$$BP = \alpha_{air-ST} \cdot AP_{air-ST} + \alpha_{air-TM} \cdot AP_{air-TM} + \alpha_{ST-TM} \cdot AP_{ST-TM} \tag{3.36}$$

where

$$\alpha_{air-ST} + \alpha_{air-TM} + \alpha_{ST-TM} = 1 . \tag{3.37}$$

In this paper, we used uniform weights  $\alpha_{air-ST} = \alpha_{air-TM} = \alpha_{ST-TM} = \frac{1}{3}$  as we assume that three materials evenly contribute to the CT density at an arbitrary voxel in T-junction, without any predominance. When using uniform weights, the  $BP$  is determined as the center of the triangle formed by three  $AP$ s [see Figure 3.10(b)]



$$\begin{aligned}
BP &= \frac{1}{3} \cdot (AP_{air-ST} + AP_{air-TM} + AP_{ST-TM}) \\
&= \frac{t_{air/(air-ST)} + t_{air/(air-TM)}}{3} \cdot C_{air} + \frac{t_{ST/(air-ST)} + t_{ST/(ST-TM)}}{3} \cdot C_{ST} \\
&\quad + \frac{t_{TM/(air-TM)} + t_{TM/(ST-TM)}}{3} \cdot C_{TM}
\end{aligned} \tag{3.38}$$

where

$$t_{air/(air-ST)} + t_{ST/(air-ST)} + t_{air/(air-TM)} + t_{TM/(air-TM)} + t_{ST/(ST-TM)} + t_{TM/(ST-TM)} = 3. \tag{3.39}$$

The position of  $BP$  is determined by the areas of three sub-triangles, which is proportional to the fraction of each material. Therefore, the material fractions of air, ST, and TM in T-junction can be estimated as follows:

$$\begin{aligned}
t_{air/T-junction} &= \frac{t_{air/(air-ST)} + t_{air/(air-TM)}}{3}, \\
t_{ST/T-junction} &= \frac{t_{ST/(air-ST)} + t_{ST/(ST-TM)}}{3}, \\
t_{TM/T-junction} &= \frac{t_{TM/(air-TM)} + t_{TM/(ST-TM)}}{3} = 1 - t_{air/T-junction} - t_{ST/T-junction}.
\end{aligned} \tag{3.40}$$

For the three-material model in material fraction space as a barycentric coordinate on triangle, the estimation of the three-material fractions can be considered as a problem of determining a  $BP$  in the interior of the triangle. To determine the  $BP$  without any ambiguity, Serlie *et al.* [36] represented the orthogonal projection of the data measurement triplet  $(I, \theta_1 \sigma_\omega I_\omega, \theta_2 \sigma_\omega^2 I_{\omega\omega})$  including the second derivative term and implemented the orthogonal projection in a numerical manner by using the code-book due to the high computational complexity of the projection. On the other hand, in this paper, we proposed a new

projection method, in which data measurement pair  $(I, \theta \sigma_\omega I_\omega)$  excluding the second derivative term is not projected directly on the three-material model but projected three times on three possible pairs of two-material models. The barycentric interpolation of the three pairs of two-material fractions simply determines a single  $BP$  without any ambiguity. By converting the projection for the three-material model into that for the two-material model, our new projection method provides a very quick estimate of the three-material fractions without the use of code-book.

In Serlie *et al.*'s orthogonal projection [36], despite of the use of the code-book, it still takes too much computation time because the data measurements for each voxel should be compared to all of the entries in the code-book. Besides, based on a tradeoff between the sampling ratio of code-book generation and the precision of the estimated three-material fractions, when we decreases the sampling ratio to establish a more accurate estimation, the growth of code-book makes the processing time for the comparison of all of the entries in the code-book increase critically. On the other hand, in our new projection method, the orthogonal projection for two-material model, which requires far less computation time compared to that of the three-material model, is used to accelerate the estimation of the three-material fractions. In addition, it does not require any additional memory storage and computational effort to generate the code-book.

Unlike the previous three-material model that approximates three-material fractions as one of the entries in the pre-generated code-book, the proposed model provides a very quick estimate of the three-material fractions without the use of the code-book. In our three-material model, three pairs of two-material fractions are

calculated by using the two-material transition model and then simply combined into a single triple of three-material fractions based on the barycentric interpolation in material fraction space. Considering that the code-book of the previous three-material model is generated by uniformly sampling the model representation in material fraction space, the temporal resolution of the sampling limits the precision of the estimated three-material fractions in the previous model, whereas it does not in our model.

## Chapter 4. Structural Response

### 4.1 Overview

Although material fractions are used to mitigate the PV effect, ST structure degradation due to the pseudo-enhancement effect still remains unresolved. For the preservation of the submerged folds and polyps, we use rut- and cup-enhancement functions designed by Cai *et al.* [38] to enhance the submerged folds and polyps, respectively, based on local structural features rather than CT density values.

### 4.2 Eigenvalue signature of folds and polyps

Let  $I(\mathbf{x})$  denote the CT density value at a point  $\mathbf{x} = (x, y, z) \in \mathbb{R}^3$  in a CT volume. The local structure of  $I(\mathbf{x})$  in a neighborhood of  $\mathbf{x}$  can be approximated by the Taylor expansion

$$I(\mathbf{x} + d\mathbf{x}) = I(\mathbf{x}) + g(\mathbf{x})d\mathbf{x} + \frac{1}{2}H(\mathbf{x})(d\mathbf{x})^2, \quad (4.1)$$

where  $g(\mathbf{x})$  and  $H(\mathbf{x})$  denote the gradient vector and the Hessian matrix, respectively.  $g(\mathbf{x})$  and  $H(\mathbf{x})$  are calculated by the convolution of the partial first and second derivatives of a Gaussian function and  $I(\mathbf{x})$ :

$$g(x) = \begin{bmatrix} \frac{\partial I}{\partial x} & \frac{\partial I}{\partial y} & \frac{\partial I}{\partial z} \end{bmatrix}, \quad (4.2)$$

$$H(x) = \begin{bmatrix} \frac{\partial^2 I}{\partial x^2} & \frac{\partial^2 I}{\partial x \partial y} & \frac{\partial^2 I}{\partial x \partial z} \\ \frac{\partial^2 I}{\partial y \partial x} & \frac{\partial^2 I}{\partial y^2} & \frac{\partial^2 I}{\partial y \partial z} \\ \frac{\partial^2 I}{\partial z \partial x} & \frac{\partial^2 I}{\partial z \partial y} & \frac{\partial^2 I}{\partial z^2} \end{bmatrix} \quad (4.3)$$

where  $\frac{\partial I}{\partial a} \equiv \left[ \frac{\partial}{\partial a} G(x; \sigma) \right] * I(x)$  and  $\frac{\partial^2 I}{\partial a \partial b} \equiv \left[ \frac{\partial^2}{\partial a \partial b} G(x; \sigma) \right] * I(x)$ .

Let the eigenvalues of Hessian matrix  $H$  be  $\lambda_1$ ,  $\lambda_2$ , and  $\lambda_3$  ( $|\lambda_1| \leq |\lambda_2| \leq |\lambda_3|$ ), and their corresponding eigenvectors be  $e_1$ ,  $e_2$ , and  $e_3$ , respectively. The local morphologic structure of an object can be characterized by use of a combination of the eigenvalues of the Hessian matrix, called eigenvalue signatures. In this section, we exploit the eigenvalue signatures of fold and polyp structures submerged in the TMs to preserve them in the cleansed images.

In the colonic lumen, polyps tend to appear as bulbous, cap-like structures that adhere to the colonic wall; folds appear as elongated, ridge-like structures; and the colonic wall appears as a large, nearly flat, cup-like structure [see Figure 4.1]. Morphologically, when folds and polyps are submerged in the TMs, they present rut-like (concave ridge) and cup-like (concave cap) shapes, because the TMs usually have higher CT values than do those for ST structures.

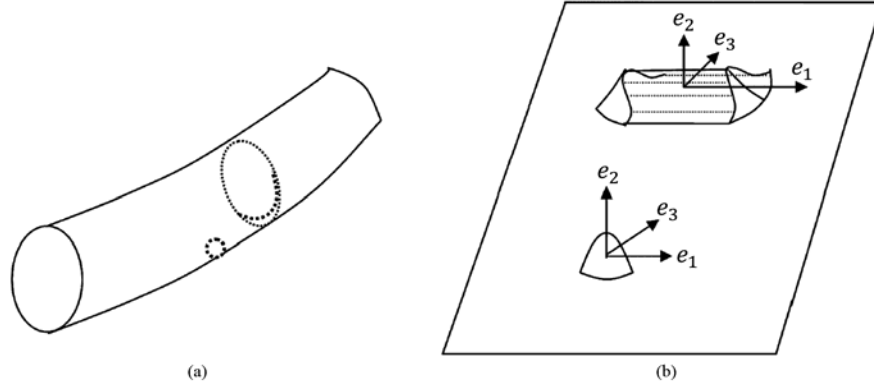


Figure 4.1 Morphologic shapes of a haustral fold and a colonic polyp. (a) Schematic illustration of the fold, the polyp, and the colonic wall. (b) Planar surface of the colon. The fold is depicted as a ridge-like structure, whereas the polyp is depicted as a cap-like structure. The three vectors  $e_1$ ,  $e_2$ , and  $e_3$  represent the eigenvectors of the Hessian matrix for the fold and the polyp.

Figure 4.2 shows a fold in a phantom submerged in the TMs. The profiles show the change in CT density values and eigenvalues of the Hessian matrix along the short and long axes on the cross-sectional image of the fold. Along the short axis, the CT density values and the eigenvalues of the Hessian matrix were calculated and sampled by an interval of one voxel. The resulting CT density profile demonstrates the PEH effect; the fold, for which the CT density value is originally approximately 50 HU, is enhanced up to 600 HU. We observe that the maximum eigenvalue  $\lambda_3$  changes from negative to positive, and then to negative again (i.e., the local structure in CT images changes from convex to concave, and then to convex again) along the sampling line. The convex structure corresponds to the transition from the TMs (bright foreground) to the fold (dark background), whereas the concave structure corresponds to the transition from the fold (dark foreground) to the TMs (bright background). We are interested only in the latter shape, i.e., that

of the local structures for which  $\lambda_3 > 0$ .

In the range of  $\lambda_3 > 0$ , we observe that the minimum eigenvalue  $\lambda_1$  is close to zero; this indicates that there is no change in curvature along the central axis because the direction of the eigenvector  $e_1$  corresponds to the central axis of the fold. Eigenvectors  $e_2$  and  $e_3$ , which are perpendicular to  $e_1$ , are on the plane perpendicular to the central axis of the fold, and they correspond to the long and short axes, respectively. Suppose that the thickness of a fold is substantially smaller

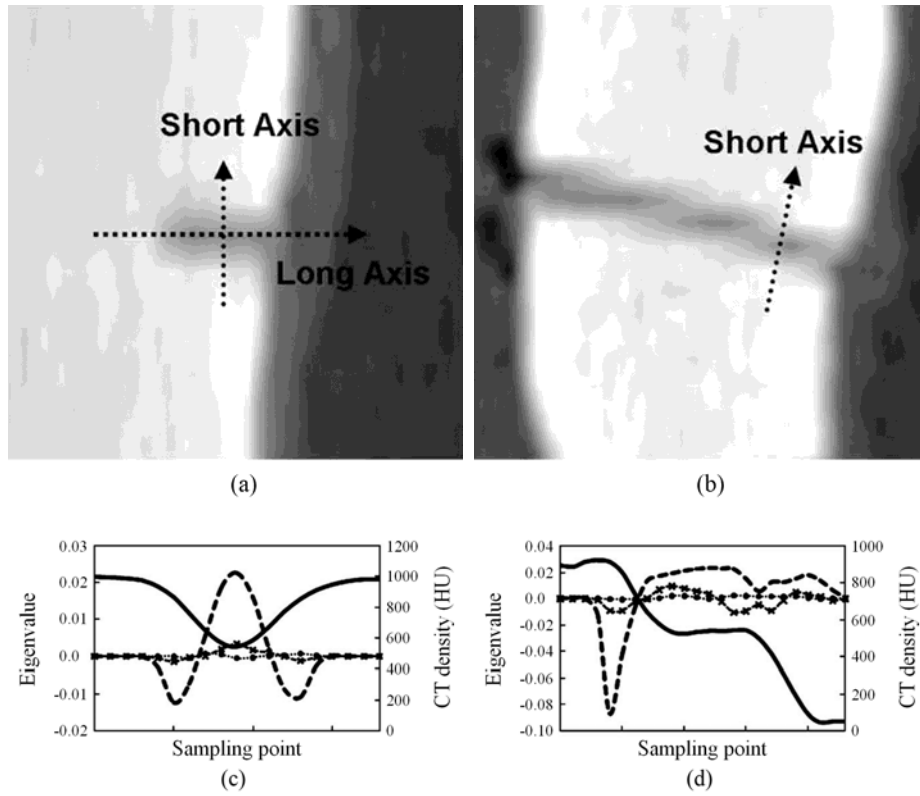


Figure 4.2 Profiles of a submerged fold on a colon phantom. (a) Two sampling lines on the cross-sectional image of a fold. (b) Coronal view of the fold in (a). (c) Plot of the change in CT density values and eigenvalues of the Hessian matrix along the short axis in (a). (d) Plot of the change in CT density values and eigenvalues of the Hessian matrix along the long axis in (a).

than its height. Then,  $\lambda_2$  and  $\lambda_3$  are inversely proportional to the height and the thickness of the fold, respectively. Along the short and long axes,  $\lambda_1$  is close to zero and  $\lambda_3$  stays positive in the region of the axis in the fold area, whereas  $\lambda_2$  changes from positive to negative. This change implies that the background structures changed from TMs to the colonic wall and  $\lambda_2$  varies with the height of the fold relative to the background. Therefore, submerged folds are characterized by an eigenvalue signature of  $\lambda_3 > 0$ ,  $\lambda_1 \approx 0$ , and  $\lambda_2 \ll \lambda_3$ .

Figure 4.3 shows a polyp in a phantom submerged in the TMs. The profiles show the change in CT density values and eigenvalues of the Hessian matrix along the sampling line of the polyp. The region with  $\lambda_3 > 0$  indicates the polyp region. It should be noted that all eigenvalues are zero in the middle of the polyp (around point 15). In this region, the kernel for computing the second derivative of the CT values is located completely within the ST region, in which the CT profile varies very little. In the region where  $\lambda_3 > 0$ ,  $\lambda_1$ ,  $\lambda_2$ , and  $\lambda_3$  are roughly linearly proportional, and they are comparable in magnitude. Therefore, polyps submerged in the TMs are characterized by an eigenvalue signature of  $\lambda_3 > 0$ ,  $\lambda_1 \approx \lambda_2$ , and  $\lambda_2 \propto \lambda_3$ .



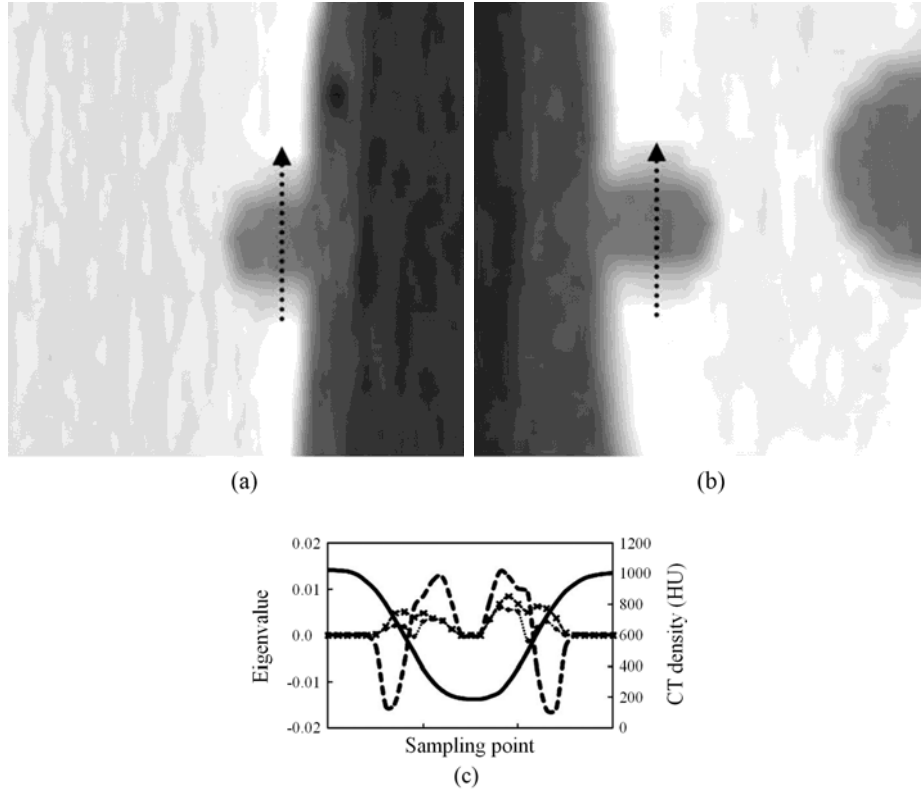
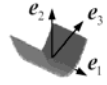
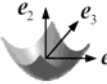


Figure 4.3 Profiles of a submerged polyp on a colon phantom. (a) A sampling line on the cross-sectional image of a polyp. (b) Coronal view of the fold in (a). (c) Plot of the change in CT density values and eigenvalues of the Hessian matrix along the sampling line in (a).

These relationships among eigenvalues build up the eigenvalue signatures that are characteristic of folds and polyps submerged in TMs, as shown in Table 4.1.

Table 4.1 Eigenvalue signatures of fold and polyp submerged in the tagged materials

Anatomic example	Morphological category	Eigenvalue signature
Submerged fold	 Rut	$\lambda_3 > 0$ , $\lambda_1 \approx 0$ , and $\lambda_2 \ll \lambda_3$
Submerged polyp	 Cup	$\lambda_3 > 0$ , $\lambda_1 \approx \lambda_2$ , and $\lambda_2 \propto \lambda_3$

### 4.3 Structural response of folds and polyps

Based on the eigenvalue signatures, two structural enhancement functions are designed to enhance the rut-like (i.e., submerged fold) and the cup-like (i.e., submerged polyp) structures.

#### 4.3.1 Rut-enhancement function for submerged folds

The first is the rut-enhancement function  $F_{rut}$ , defined as

$$F_{rut} = F_A \cdot F_B \quad (4.4)$$

where  $F_A$  and  $F_B$  are discrimination functions to uplift rut-like structures.

The discrimination function  $F_A$  differentiates between an elongated object and a sphere object

$$F_A = \exp\left(-\frac{R_a^2}{2\alpha^2}\right), \quad R_a = \frac{|\lambda_1|}{\sqrt{\lambda_2\lambda_3}}. \quad (4.5)$$

This function reflects a part of the eigenvalue signature in Table 3.I:  $\lambda_1 \approx 0$  ( $|\lambda_1| \ll |\lambda_2|$  and  $|\lambda_1| \ll |\lambda_3|$ ). It takes a maximum value when  $\lambda_1$  approaches zero, that is, when the underlying object has an elongated structure. It takes a minimum value when  $\lambda_1 = \lambda_2 = \lambda_3$ , that is, when the underlying object has a spherical structure. The range of the function is controlled by the parameter  $\alpha < 1$ .

Changes in the value of the discrimination function  $F_A$  as a function of  $R_a$  at different value of  $\alpha$  are shown in the curves in Figure 4.4(a). Figure 4.4(b) shows a coronal image of the colonic phantom, in which all the voxels above 200 HU are

shaded. We observe that parts of the folds and polyps are pseudo-enhanced. The response images of the phantom resulting from the application of the discrimination function  $F_A$  at different values of  $\alpha$  are shown in Figure 4.4(c). The submerged structures, especially the thin folds, are enhanced at different scales with different  $\alpha$  values. A small value of  $\alpha$  narrows the enhancement range of folds, whereas a large value of  $\alpha$  enlarges the enhancement range. In order to balance the level of enhancement with noise and other structures, we selected  $\alpha = 0.5$  in our study.

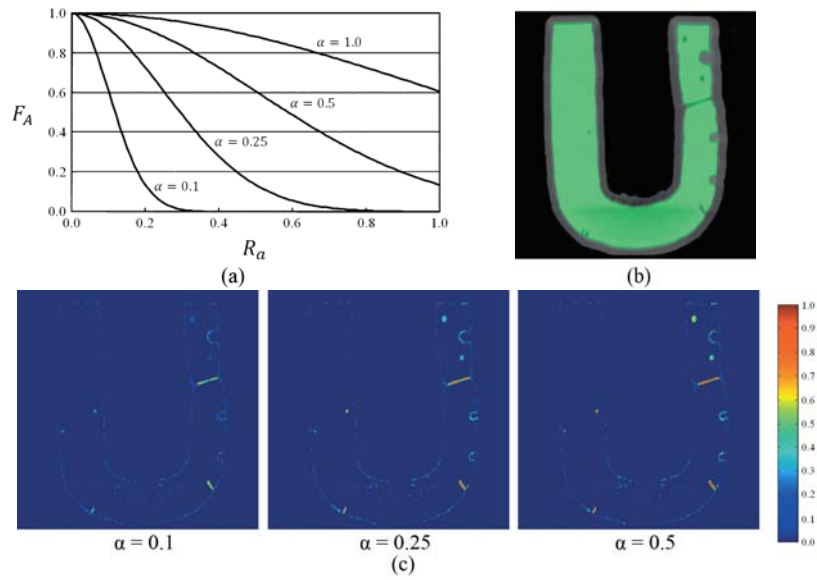


Figure 4.4 Effect of discrimination function  $F_A$  on the differentiation of folds from other structures in the colon phantom. (a)  $F_A$  as a function of  $R_a$  at different values of  $\alpha$ . (b) Coronal view of the CTC images of a colon phantom. All voxels above 200 HU are shaded. (c) Response images of the phantom image resulting from the application of  $F_A$  at  $\alpha = 0.1$ ,  $\alpha = 0.25$ , and  $\alpha = 0.5$ .

The discrimination function  $F_B$  characterizes the cross-sectional structure of a rut, or the crest shape, on the plane perpendicular to the central axis of the rut, and thus it depends only on the ratio of  $\lambda_2$  to  $\lambda_3$ , as follows:

$$F_B = \exp\left(-\frac{(R_b - \gamma)^2}{2\beta^2}\right), \quad R_b = \frac{|\lambda_2|}{|\lambda_3|}. \quad (4.6)$$

This function reflects a part of the eigenvalue signature in Table 3.I:  $\lambda_2 \propto \lambda_3$ . The range of the function is controlled by the parameter  $\beta < 1$ .  $R_b = 0.0$  represents a plate-like structure, whereas  $R_b = 1.0$  represents a structure with a circular section. Thus, the function  $F_B$  enhances structures between these two shapes.

Changes in the value of the discrimination function  $F_B$  as a function of  $R_b$  at different values of  $\beta$  and  $\gamma$  are shown in the curves in Figures 4.5(a) and 4.5(b). Figures 4.5(c) and 4.5(d) show the response images of the phantom [see Figure 4.5(b)] resulting from the application of the discrimination function  $F_B$  with  $\gamma = 0.2$  and  $\gamma = 0.3$ , respectively. To balance the side effect from the enhancement of plate and sphere, we selected the values  $\beta = 0.3$  and  $\gamma = 0.3$  in our study.

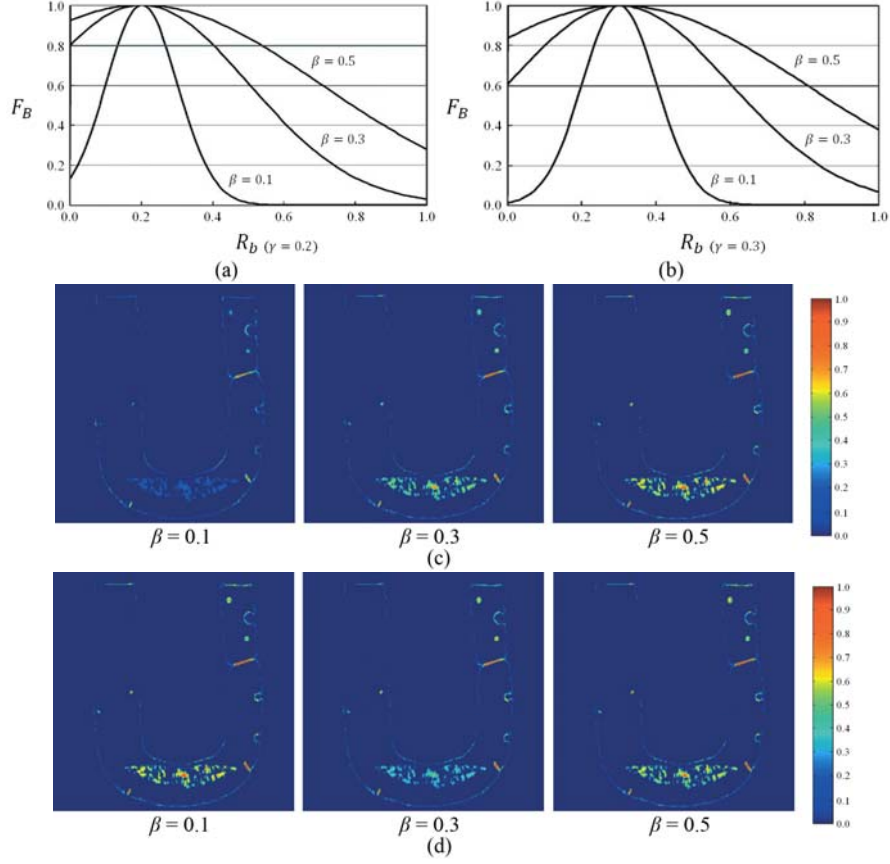


Figure 4.5 Effect of discrimination function  $F_B$  on the differentiation of folds from other structures in the colon phantom. (a), (b)  $F_B$  as a function of  $R_b$  at different values of  $\beta$  and at the fixed values of  $\gamma = 0.2$  and  $\gamma = 0.3$ . (c), (d) Response images of the phantom image resulting from the application of  $F_B$  at  $\beta = 0.1$ ,  $\beta = 0.3$ , and  $\beta = 0.5$  with  $\gamma = 0.2$  and  $\gamma = 0.3$ .

### 4.3.2 Cup-enhancement function for submerged polyps

The second structural enhancement function is a cup-enhancement function  $F_{cup}$

to uplift the cup-like structure (i.e., the submerged polyp structure) defined by

$$F_{cup} = F_C(\lambda_1, \lambda_2) \cdot F_C(\lambda_2, \lambda_3) \quad (4.7)$$

with

$$F_C(\lambda_i, \lambda_j) = 1.0 - \exp\left(-\frac{R_c^2}{2\eta^2}\right), \quad R_c = \frac{|\lambda_i|}{|\lambda_j|}. \quad (4.8)$$

The parameter controls the range of the enhancement function  $F_C$  as illustrated in Figure 4.6. Because most polyps are not strictly spherical in shape, we selected  $\eta = 0.2$  in this study.

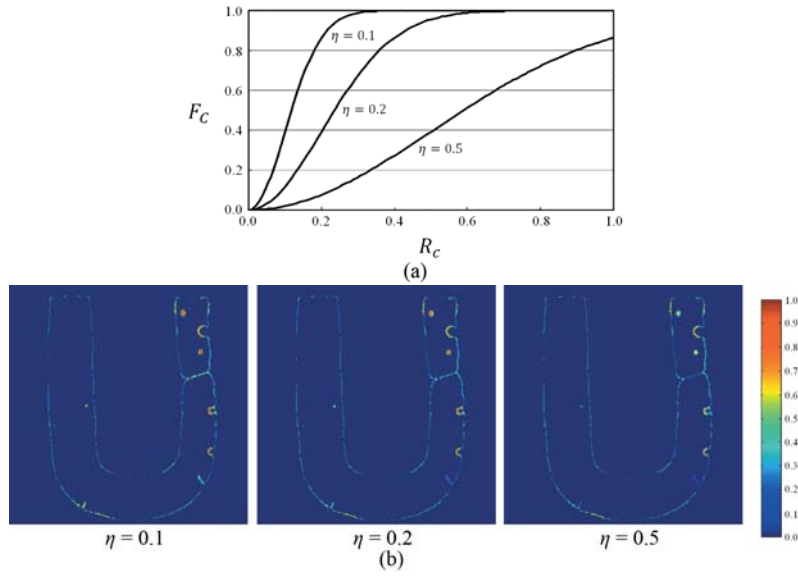


Figure 4.6 Effect of discrimination function  $F_C$  on the differentiation of polyps from other structures in the colon phantom. (a)  $F_C$  as a function of  $R_c$  at different values of  $\eta$ . (b) Response images of the phantom image resulting from the application of  $F_C$  at  $\eta = 0.1$ ,  $\eta = 0.2$ , and  $\eta = 0.5$ .

By calculating the values of the rut- and cup-enhancement functions on each of the voxels in the TMs that satisfy  $\lambda_3 > 0$ , the structures exposed in the air lumen are excluded. The maximum value of the two enhancement functions is assigned as a structural response  $H_\Lambda$  at point  $x$

$$H_\Lambda(x) = \max \{F_{rut}(x), F_{cup}(x)\}. \quad (4.9)$$

Figure 4.7 shows images of the structural response of a colon resulting from the two enhancement functions for folds and polyps to a clinical CTC case. The submerged folds and polyps are well enhanced, whereas the other structures, such as TMs, air bubbles, folds in the air lumen, and the colonic wall, are de-enhanced.

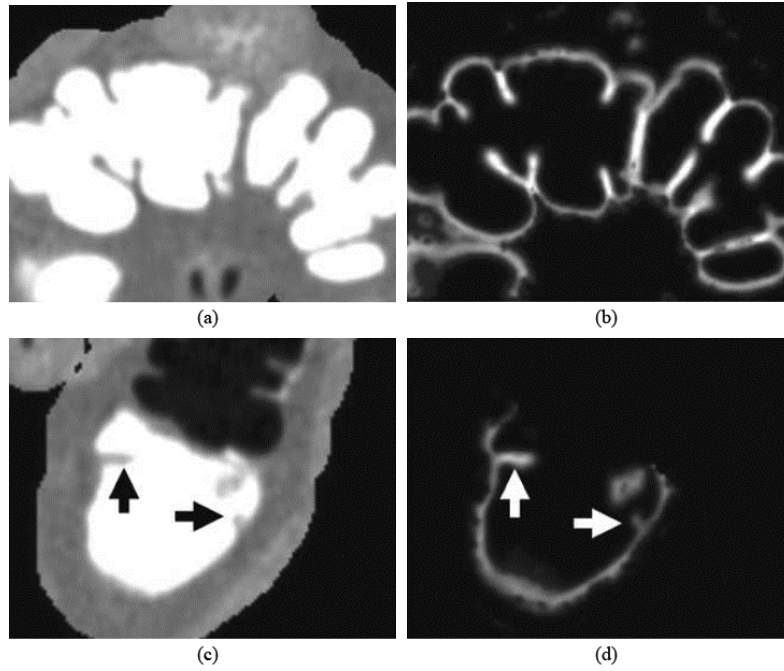


Figure 4.7 Demonstration of the effect of the structural enhancement functions on folds and polyps. (a), (c) Portion of the colonic lumen filled with TMs. (b), (d) Result of the structural response to the lumen in (a) and (c). The folds and polyps submerged in the TMs are well enhanced.

## Chapter 5. Reconstruction Model

### 5.1 Overview

Finally, in the last step, also called reconstruction of the transition layer, CT density value of each voxel in colonic regions is reconstructed based on the material fractions and structural responses. In air, TM, and  $IL_{air/TM}$ , the CT density values of voxels are simply replaced by  $I_{air}$ , because there is no contribution of PV of ST in these regions and TM would be eventually replaced with air regardless of material fractions at each voxel. On the other hand, each voxel in  $IL_{ST/TM}$  and T-junction is reconstructed based on our new reconstruction model, which simultaneously considers the material fractions and the structural responses.

### 5.2 Material fraction-based reconstruction model

Let us first consider material fractions-based reconstruction model. As described in Section 3.3.1, a CT density of a voxel in T-junction can be modeled as a linear combination of pure material densities of air, ST, and TM with corresponding their material fractions:  $I = t_{air} \cdot I_{air} + t_{ST} \cdot I_{ST} + t_{TM} \cdot I_{TM}$ . A CT density of a voxel in  $IL_{ST/TM}$  corresponds to the special case that  $t_{air} = 0$ , in which there is no contribution of PV of air. The material fractions-based reconstruction model changes CT density value at each voxel by replacing the contributions of TM with



air based on the material fractions in the voxel

$$I_{material-fraction} = t_{air} \cdot I_{air} + t_{ST} \cdot I_{ST} + t_{TM} \cdot I_{air} . \quad (5.1)$$

### 5.3 ST-preserving reconstruction model

In order to resolve the erroneous cleansing of the submerged folds and polyps due to PEH effect, we propose a new reconstruction model by integrating the structural response into the material fractions-based reconstruction model (3.52). Considering that the structural response value, which is in the range of 0 and 1, indicates the probability that the voxel is within a submerged fold or polyp, the reconstructed CT density value of the voxel having a higher structural response value needs to be closer to the original CT density  $I$ . Therefore, we present a ST-preserving reconstruction model, in which the final CT density  $I_{ST-preserving}$  is reconstructed by considering simultaneously the CT density  $I_{material-fractions}$  obtained by the material fractions-based reconstruction model and the original CT density value  $I$  with the weight factor of structural response as follows

$$\begin{aligned} I_{ST-preserving} &= \left(1 - (1 - H_{\Lambda})^{\kappa}\right) \cdot I + (1 - H_{\Lambda})^{\kappa} \cdot I_{material-fractions} \\ &= t_{air} \cdot I_{air} + t_{ST} \cdot I_{ST} + t_{TM} \cdot \left\{ \left(1 - (1 - H_{\Lambda})^{\kappa}\right) \cdot I_{TM} + (1 - H_{\Lambda})^{\kappa} \cdot I_{air} \right\} . \end{aligned} \quad (5.2)$$

Let  $H_{\Lambda}$  represent the structural response value at each voxel. The parameter  $\kappa$  controls the relative contribution of the structural response to the ST preservation. In this paper, the parameter  $\kappa$  is experimentally set as 2.

With the use of structural responses as well as material fractions to reconstruct the CT density values, the ST-preserving reconstruction model does not simply replace the contributions of TM with air, but with the combination of air and TM. The structural response controls the relative contributions of air and TM in our reconstruction model. As the structural response at a voxel in the submerged folds and polyps increases the contribution of TM thus reduces the replacement of TM with air, the reconstructed CT density of the voxel is enhanced. This increment of the CT density resolves PEH effect. Therefore, using the ST-preserving reconstruction model, the submerged folds and polyps are well preserved without ST structure degradation due to PEH effect.

## Chapter 6. Experiments

### 6.1 Data preparation

For the performance evaluation of the proposed EC method, we used clinical CT datasets from 10 patients. Each patient was scanned at both supine and prone positions, so a total of 20 scans were acquired. CT scanning was performed with 64-row multidetector CT scanner (Brilliance 64, Philips Medical Systems, Cleveland, OH). Each scan had more than 600 slice images with a matrix size of  $512 \times 512$  and the pixel size ranged from 0.54 to 0.68 mm. Scans were reconstructed with slice thickness of 1 mm and interval of 0.7 mm. Other scanning parameters were as follows: detector collimation of  $16 \times 0.625$  mm, 1.172 pitch, gantry rotation time of 0.72 s, 50 effective mAs, and 120 kVp. Intravenous contrast administration was not performed.

All patients had the following bowel preparation. Three to four days prior to the CT examination, patients were asked to refrain from foods that were rich in fiber, seeded fruits, and seaweed. At one day before the examination, patients had a regular diet for breakfast and rice porridge for lunch. No dinner was allowed. Colonic cleansing was performed using one pack of magnesium citrate powder (LosoPrep<sup>®</sup>, EZ-EM Inc.) and 20 mg of bisacodyl tablets (Dulcorax<sup>®</sup>, EZ-EM Inc.). A 10 mg bisacodyl suppository was inserted in the patients' rectum to evacuate colonic fluid at 30 min before the examination. For fecal tagging, a combination of barium and iodinated contrast material (Gastrografin<sup>®</sup>, Bayer-Schering, Berlin,

Germany) was used. Of the five patients, nine patients received 60 ml of 40% w/v barium suspension (Tagitol V<sup>®</sup>, EZ-EM Inc., Lake Success, NY) and the remaining one patient received 600 ml of 4.6% w/v barium suspension (EasyCT<sup>®</sup>, TaeJoon Pharm., Seoul, Korea). However, the total amount of barium for the two suspensions was similar: 24.0 g and 27.6 g, respectively. The patients were also asked to take 50 ml of gastrografen at four hours before the examination.

## **6.2 ST-preserving reconstruction model**

To evaluate the performance of the ST-preserving reconstruction model, we compared the results of our EC method with those of material fractions-based EC method [35] having no ST-preserving weight factor. The EC results using our method with the ST-preserving weight factor and previous method [35] without the ST-preserving weight factor were denoted by EC<sub>prev</sub> and EC<sub>our</sub>, respectively.

### **6.2.1 Cleansing quality**

For the subjective evaluation, the cleansing quality was visually assessed by an abdominal radiologist with clinical experience of more than 1,000 CTC cases. From the original CT datasets and two electronically cleansed CT datasets (i.e., EC<sub>prev</sub> and EC<sub>our</sub>), 3D volume-rendered images of panoramic endoluminal view (referred to hereafter as “band view”) were generated by navigating through the colon lumen on a 3D workstation (Xelis Colon, INFINITT, Seoul, Korea) [50]. The

band view images from both  $EC_{prev}$  and  $EC_{our}$  were displayed vertically on the same screen with a random order (i.e., one on the top and the other on the bottom) while the band view image from original dataset was also displayed on the middle for reference. During the navigation, for each tagged pool containing at least one submerged fold or polyp, the radiologist rated the cleansing quality to each of the top and bottom images on a 4-point scale in a blind manner to guarantee the objectivity of the subjective analysis to the best [see Table 6.1]. And, in a case of a tagged pool rated as grade 1 or 2, the radiologist also determined the reason for the low quality of EC as one of five possible causes [see Table 6.2].

Table 6.1 Grading scheme in cleansing quality evaluation

Cleansing quality grade	
1	Inadequate (nondiagnostic colon with severe EC-related artifact)
2	Moderate (diagnostic colon with moderate EC-related artifact)
3	Good (diagnostic colon with mild EC-related artifact)
4	Excellent (diagnostic colon without EC-related artifact)

Table 6.2 Five causes for the low quality of EC

Reasons for poor EC	
1	Artifacts at T-junctions
2	Inhomogeneous tagging
3	Collapsed area
4	Image noise
5	Incomplete EC

Figure 6.1 compares the 3D band view images containing submerged folds from the original,  $EC_{prev}$ , and  $EC_{our}$  datasets. The submerged folds are covered by TMs before EC [see Figure 6.1(a)], but they become clearly visible after EC in both of  $EC_{prev}$  and  $EC_{our}$  [see Figure 6.1(b)-(e)]. Both methods of  $EC_{prev}$  and  $EC_{our}$  showed a good result of electric cleansing without the aliasing artifacts between ST and TM. However, with  $EC_{prev}$ , the submerged folds had a rough surface [see Figure 6.1(b)] or became excessively cleansed [see Figure 6.1(d)], demonstrating that the previous method only using the material fractions does not cope with the inappropriately enhanced density of the submerged folds from PEH effect. In contrast,  $EC_{our}$  exploiting both the material fractions and structural responses preserved the submerged folds well while resolving the aliasing artifacts between ST and TM [see Figures 6.1(c) and (e)].

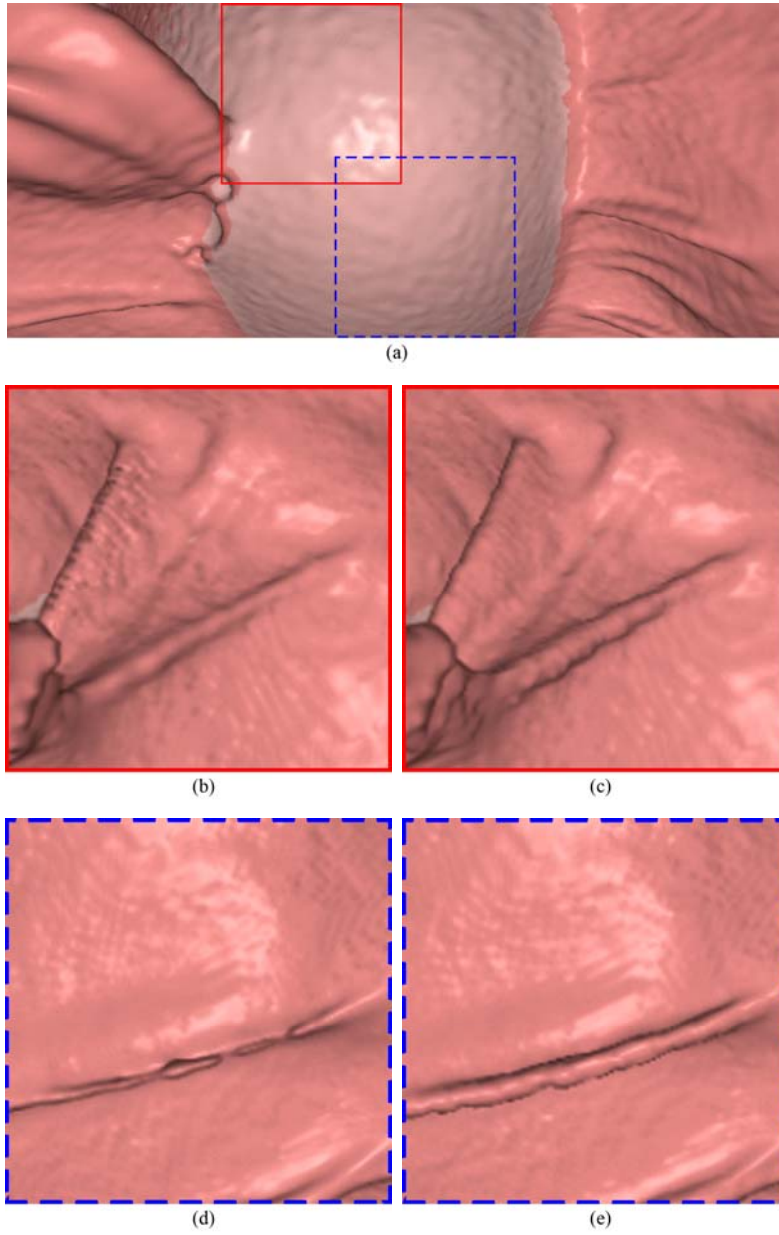


Figure 6.1 Comparison of 3D band view images from  $EC_{prev}$  and  $EC_{our}$ . (a) Band view image generated from the original dataset before EC. (b), (d) Magnified images of submerged folds from  $EC_{prev}$ . (c), (e) Magnified images of submerged folds from  $EC_{our}$ .

Figure 6.2 shows the distribution of quality grades for tagged pools of  $EC_{prev}$  and  $EC_{our}$ , for individual 10 scans. Six of 10 scans showed overall higher grades in  $EC_{our}$  than  $EC_{prev}$ , while the remaining four scans showed the same grades both in  $EC_{prev}$  and  $EC_{our}$ . For total 143 tagged pools, the average grades of cleansing quality were 2.63 and 2.76 for  $EC_{prev}$  and  $EC_{our}$ , respectively, not showing a significant difference ( $p=0.0821$ ). It might be attributed to the fact that a large number of tagged pools (68.5%, 98/143) were rated as the same grades, especially grade 3 or 4, in  $EC_{prev}$  and  $EC_{our}$ . To evidence the advantage of  $EC_{our}$  over  $EC_{prev}$  in cleansing quality, we additionally compared the average grades for tagged pools, which were rated as grade 1 or 2 in  $EC_{prev}$ . For these 45 tagged pools, the cleansing quality for  $EC_{our}$  was significantly higher than that for  $EC_{prev}$  ( $p=0.0001$ ). The average grade of cleansing quality was 1.73 and 2.22 for  $EC_{prev}$  and  $EC_{our}$ , respectively.

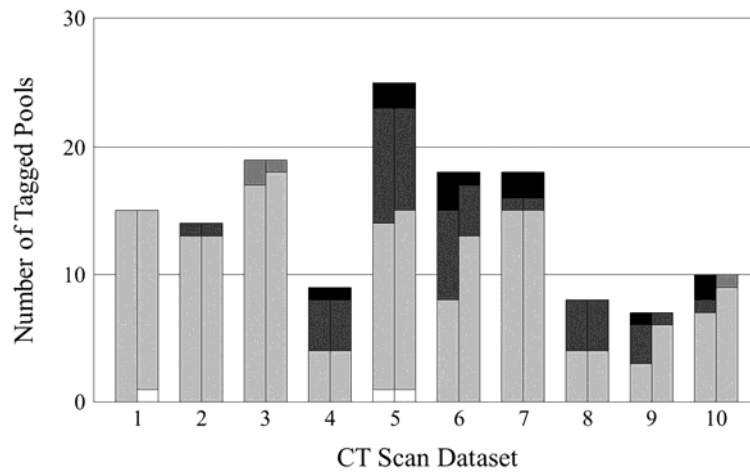


Figure 6.2 Quality grades for tagged pools determined by a radiologist for 10 scans. Two bar at each scan represent  $EC_{prev}$  (left) and  $EC_{our}$  (right). Each gray shaded color represents different quality grades: grade 1 (black), grade 2 (dark gray), grade 3 (light gray), or grade 4 (white).



Figure 6.3 shows the distribution of the reasons for the low quality of EC in  $EC_{prev}$  and  $EC_{our}$ . Compared to  $EC_{prev}$ ,  $EC_{our}$  decreased the number of tagged pools rated as grade 1 or 2 indicating the low quality of EC. Of total 143 tagged pools, 31.1% (45/143) and 23.1% (33/143) tagged pools were rated as grade 1 or 2 in  $EC_{prev}$  and in  $EC_{our}$ , respectively. The most common reason for the low quality of EC was the artifacts at T-junctions where the  $IL_{air/TM}$  meets the colon wall. The tagged pools appertaining to this reason were 60.0% (27/45) and 63.6% (21/33) in  $EC_{prev}$  and in  $EC_{our}$ , respectively. Such artifacts at T-junctions, which typically appear as distracting ridges along the line where  $IL_{air/TM}$  touches the colon wall, could be removed by using a three-material transition model.

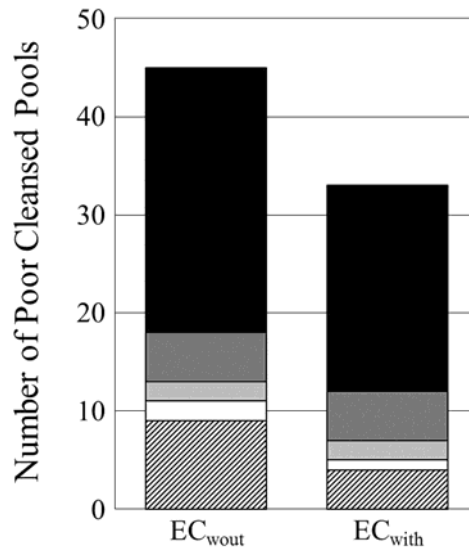


Figure 6.3 Reasons for low quality of EC. Two bar graphs represent  $EC_{prev}$  (left) and  $EC_{our}$  (right). Each gray shaded color represents five different reasons for the low quality of EC: artifacts at T-junctions (black), inhomogenous tagging (dark gray), collapsed segment (light gray), image noise (gray), and incomplete EC (oblique line).

### 6.2.2 Polyp detection

In addition to the cleansing quality, the accuracy of polyp detection before and after EC was also evaluated by the same radiologist. For five patients, eight polyps  $\geq 6$  mm were identified using OC. When both supine and prone position datasets could be considered as independent scans, there were totally 16 polyps in 10 scans. Of 16 polyps, 12 polyps were not covered by TMs, and thus were easily visible in the original,  $EC_{prev}$ , and  $EC_{our}$  datasets. The remaining four polyps, which were partially or completely covered by TMs, were not detected in the original dataset. But, all of them were clearly detected in  $EC_{prev}$  and  $EC_{our}$  datasets. Thus, the sensitivity for polyp detection after EC was identically 100% (16/16) with  $EC_{prev}$  and  $EC_{our}$ . On the other hand, the radiologist had nine and eight of false-positive polyp detections with  $EC_{prev}$  and  $EC_{our}$ , respectively. The number of false-positive detections was slightly reduced with  $EC_{our}$  than with  $EC_{prev}$ . Figure 4.4 illustrates the examples of 3D band view images containing two different types of polyps before and after EC: one partially [see Figure 6.4(a)] and the other completely [see Figure 6.4(b)] covered by TMs. Both of them were clearly visible after EC, and were confirmed to be true polyps by OC.

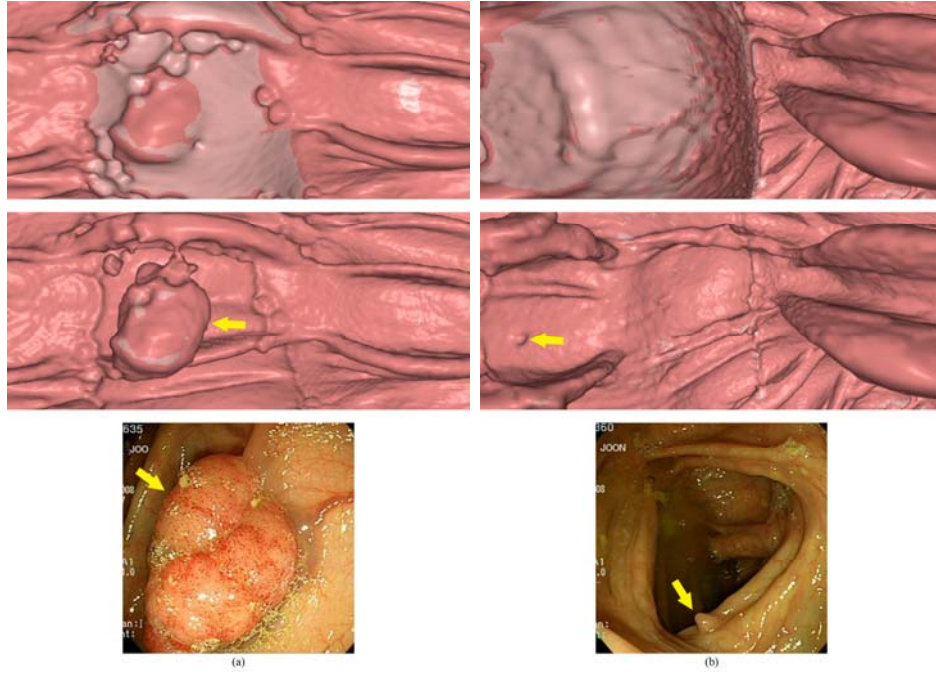


Figure 6.4 Comparison of 3D band view images from  $EC_{prev}$  and  $EC_{our}$ . (a) Band view image generated from the original dataset before EC. (b), (d) Magnified images of submerged folds from  $EC_{prev}$ . (c), (e) Magnified images of submerged folds from  $EC_{our}$ .

### 4.2.3 Manual cleansing measurement

For the objective evaluation of the proposed method, the radiologist manually segmented the submerged folds in the original datasets, and then two electronically cleansed datasets (i.e.,  $EC_{prev}$  and  $EC_{our}$ ) were compared regarding these segmented folds. By reviewing the original datasets at colon windowing setting (width, 2000 HU; level, 0 HU), the radiologist selected 10 slices per scan, which represented the submerged folds most clearly, and then manually segmented the submerged folds on the selected slices. For each segmented fold region, mean density value and fold preservation rate were measured for  $EC_{prev}$  and  $EC_{our}$ . The fold preservation rate was defined as the ratio of the number of ST voxels with density values higher than -600 HU to the total number of voxels in the segmented fold region [38].

Figure 6.5 shows the 2D slice images containing submerged folds from the original,  $EC_{prev}$ , and  $EC_{our}$  datasets. The submerged folds are covered by TMs before EC [see Figure 6.5(a)]. They are completely exposed to air after EC both in  $EC_{prev}$  and  $EC_{our}$  [see Figures 6.5(b) and (c)]. However, the submerged folds in  $EC_{prev}$  were eroded to the excessive extent as the enhanced boundary of the submerged folds was erroneously cleansed as TMs [see Figure 6.5(b)]. In contrast, the same folds in  $EC_{our}$  were preserved well [see Figure 6.5(c)], demonstrating that our fold-preserving EC method cleans TMs without degrading the ST structures submerging in TMs. For these two submerged folds, the mean density values and the fold preservation rates for  $EC_{our}$  were higher than those for  $EC_{prev}$  [see Table 6.3], supporting the visual comparison.

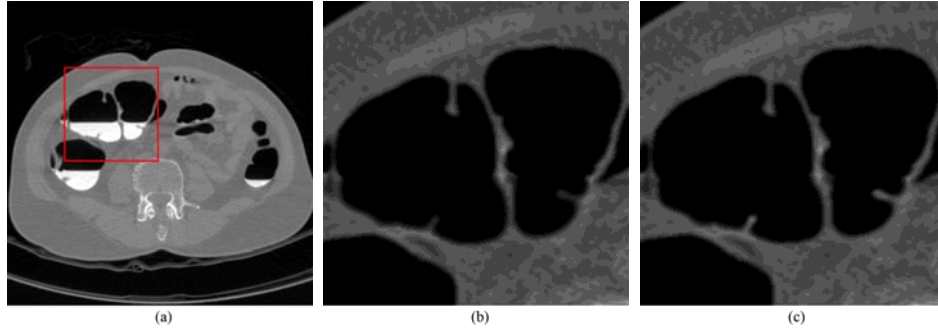


Figure 6.5 Comparison of 2D slice images from  $EC_{prev}$  and  $EC_{our}$ . (a) Original CT image. (b) Magnified image of submerged folds from  $EC_{prev}$ . (c) Magnified image of submerged folds from  $EC_{our}$ .

Table 6.3 Measurement results for two submerged folds in Figure 6.5

		$EC_{prev}$	$EC_{our}$
Mean density value (HU)	Left fold	602.8	865.8
	Right fold	530.8	810.2
Fold preservation rate (%)	Left fold	85.1	100.0
	Right fold	84.8	96.4

Figure 6.6 shows objective evaluation results for the manually segmented fold regions. The mean density value for  $EC_{our}$  was significantly higher than that for  $EC_{prev}$  ( $p < 0.0001$ ) and the fold preservation rate for  $EC_{our}$  was also significantly higher than that for  $EC_{prev}$  ( $p < 0.0001$ ). For the total 116 segmented folds, the average of mean density values were  $-305.9 \pm 126.4$  HU (mean  $\pm$  SD) and  $-181.6 \pm 83.9$  HU for  $EC_{prev}$  and  $EC_{our}$ , respectively, and the average fold preservation rates were  $88.6 \pm 9.8$  % and  $95.2 \pm 4.6$  % for  $EC_{prev}$  and  $EC_{our}$ , respectively.

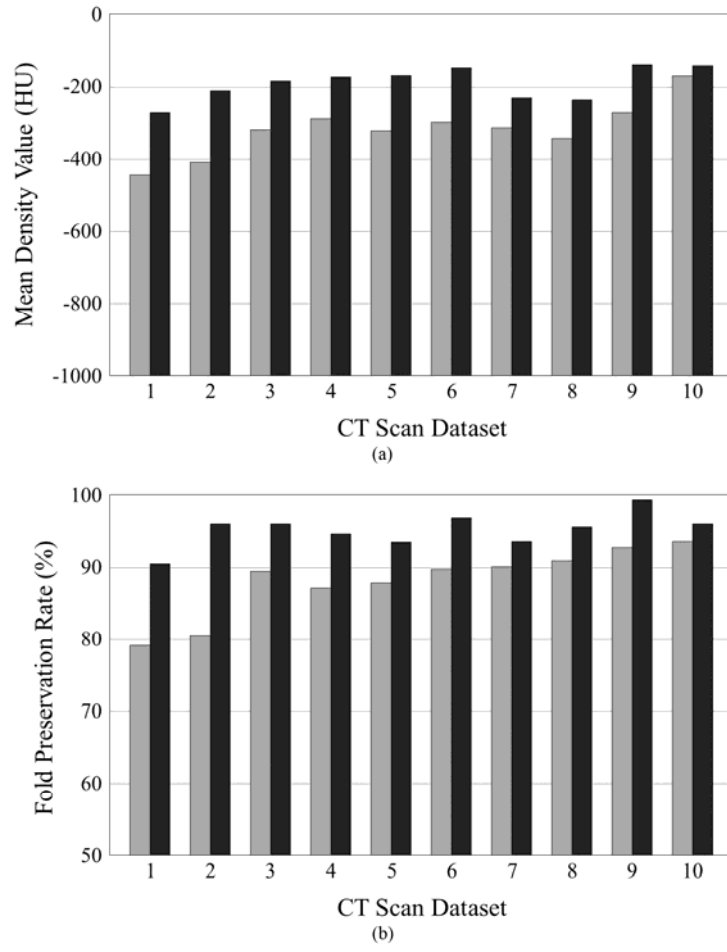


Figure 6.6 Objective evaluation results for manually segmented fold regions in 10 scans. (a) Mean density values. (b) Fold preservation rates. Two bar graphs at each scan represent  $EC_{prev}$  (left, gray) and  $EC_{our}$  (right, black).

### 6.2.4 Computational performance

To evaluate the computational performance, we compared the processing times for  $EC_{\text{prev}}$  and  $EC_{\text{our}}$ . The total processing time, averaged over 10 runs to all the datasets, were  $81.8 \pm 6.2$  s and  $96.4 \pm 11.4$  s for  $EC_{\text{prev}}$  and  $EC_{\text{our}}$ , respectively. Both  $EC_{\text{prev}}$  and  $EC_{\text{our}}$  commonly took  $76.6 \pm 5.0$  s for the segmentation of colonic components,  $4.8 \pm 1.8$  s for the estimation of material fractions, and  $0.4 \pm 0.1$  s for the reconstruction of  $IL_{\text{ST/TM}}$ . On the other hand,  $EC_{\text{our}}$  additionally required  $14.6 \pm 6.0$  s for the calculation of rut-enhancement function.

### 6.3 Fast projection for three-material model

We evaluated the improvement in EC quality when the proposed projection for the three-material model was applied into our previous ST-preserving EC method. In addition, we also evaluated the improvement in computational performance by comparing the proposed projection with the previous orthogonal projection for the three-material model [36]. The EC result using the previous ST-preserving EC method was denoted by  $EC_{\text{two}}$ , because only two-material model was adopted for estimating material fractions. On the other hand, when the ST-preserving EC method was extended by using a three-material model, the EC results using the previous three-material model [36] and our proposed three-material model were denoted by  $EC_{\text{three\_prev}}$  and  $EC_{\text{three\_prop}}$ , respectively. All algorithms were implemented in C# using Microsoft Visual Studio 2008 on an Intel i7-based 2.67 GHz CPU with 6 GB of memory.

### 6.3.1 Cleansing quality

For the subjective evaluation, the cleansing quality was visually assessed by the same radiologist participated in the previous experiment for evaluation of the ST-preserving reconstruction model. From the original CT datasets and two electronically cleansed CT datasets (i.e.,  $EC_{two}$  and  $EC_{three\_prop}$ ), 3D volume-rendered images of panoramic endoluminal view were generated [50]. Along the navigation path from the rectum to the cecum, the band view was screen-captured with uniform step size of 50.0 mm. Of 338 screen-captured images from the original 10 CT scans, 228 images were selected when at least one tagged pool appeared in the image. For each selected image from the original datasets, its corresponding two electronically cleansed images were also captured from the same camera position within each of  $EC_{two}$  and  $EC_{three\_prop}$ . The total 228 selected image pairs were shown in random order and the images from  $EC_{two}$  and  $EC_{three\_prop}$  images of each pair were displayed on the same screen in a blind manner (i.e., one on the top and the other on the bottom) with the corresponding reference image from original datasets (on the center). For each selected image pair, the radiologist independently indicated a preference for one of the top and bottom images and then rated the perceptible difference of the cleansing quality between the top and bottom images on a 3-point scale [see Table 6.4].

Table 6.4 Grading scheme in comparison of cleansing quality

Comparison scale of cleansing quality	
1	Slightly better (or worse)
2	Better (or worse)
3	Much better (or worse)



Figure 6.7 compares the 3D band view images containing T-junctions from the original,  $EC_{two}$ , and  $EC_{three\_prop}$  datasets. The parts of colon surface (i.e.,  $IL_{ST/TM}$  and T-junctions) are covered by TMs before EC [see Figure 6.7(a)] but the covered colon surface are exposed and reconstructed after EC in both of  $EC_{two}$  and  $EC_{three\_prop}$  [Figs. 6.7(b)-(e)]. Both methods of  $EC_{two}$  and  $EC_{three\_prop}$  showed a good result of EC without the ST degradation artifacts of submerged folds as well as the aliasing artifacts in  $IL_{ST/TM}$ . However, in  $EC_{two}$ , T-junction artifacts were observed as distracting ridges along the line where the  $IL_{air/TM}$  touches the colon surface, demonstrating that the previous ST-preserving EC method only using the two-material model does not cope with the three-material fractions at T-junctions [see Figures 6.7(b) and (d)]. In contrast,  $EC_{three\_prop}$  adopting our new three-material model removed the T-junction artifacts and clearly reconstructed the whole colon surface including T-junction regions [see Figures 6.7(c) and (e)].

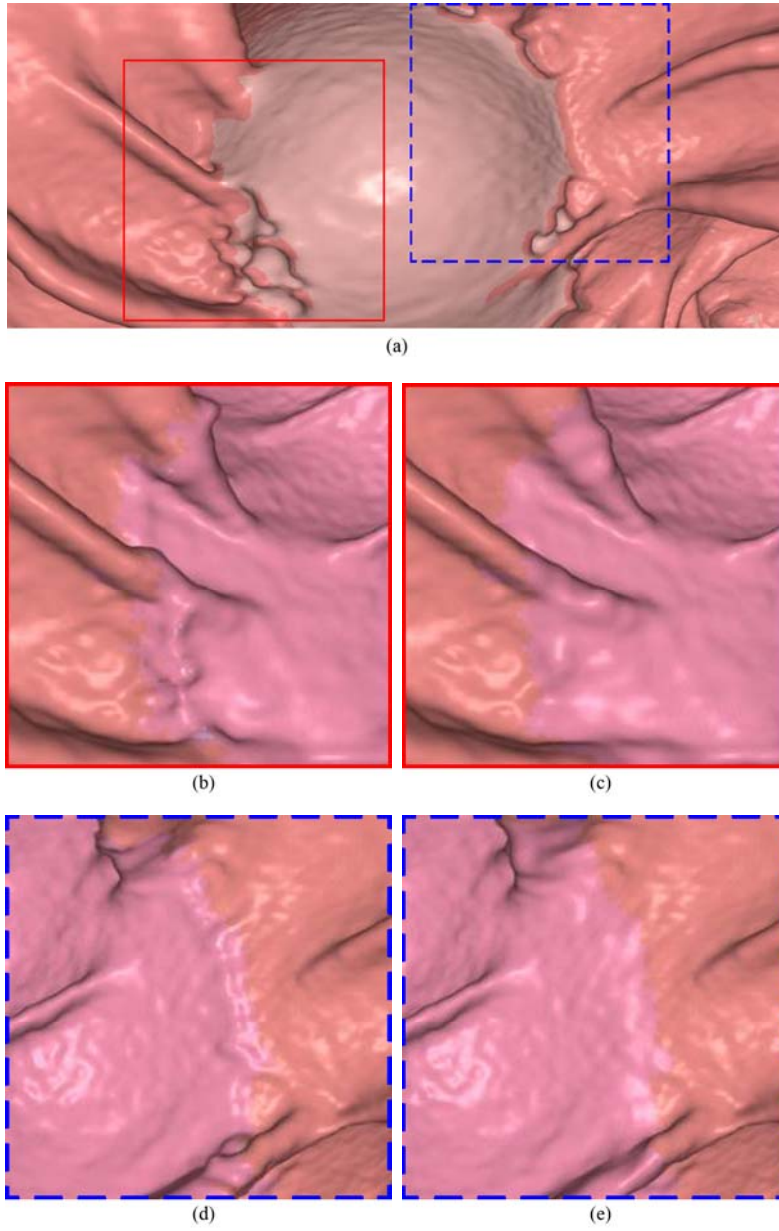


Figure 6.7 Comparison of 3D band view images from  $EC_{two}$  and  $EC_{three}$ . (a) Band view image generated from the original dataset before EC. (b), (d) Magnified images of T-junctions from  $EC_{two}$ . (c), (e) Magnified images of T-junctions from  $EC_{three}$ . The *pink coloring* indicates the part of the electronically cleansed TM regions in (b)-(e).

Table 6.5 Grading result for the perceptible difference of cleansing quality

The number of image pairs							
	Preference	Difference grade of cleansing quality					
		-3	-2	-1	1	2	3
EC <sub>two</sub>	17	0	1	16	<i>invalid</i>		
EC <sub>three</sub>	211	<i>invalid</i>			39	171	1

Table 6.5 shows the grading result for the perceptible difference of the cleansing quality between EC<sub>two</sub> and EC<sub>three\_prop</sub>. Of total 228 selected image pairs containing at least one tagged pool, the number of the preferences were 17 (7.5%, 17/228) and 211 (92.5%, 211/228) for EC<sub>two</sub> and EC<sub>three\_prop</sub>, respectively. Since the radiologist rated the difference of the cleansing quality between the top and bottom images in a blind manner, when the radiologist selected the preference for EC<sub>two</sub> images, the difference grades were considered as negative. For example, for a given image pair, if the radiologist selected the preference for EC<sub>two</sub> image and rated the difference of the cleansing quality as grade 1, the difference grade became -1 indicating that the cleansing quality of EC<sub>three\_prop</sub> is slightly “worse” than that of EC<sub>two</sub> image of the pair. And then, for total 228 image pairs, the average of the difference grades between EC<sub>two</sub> and EC<sub>three\_prop</sub> was 1.6 and this positive value yielded that EC<sub>three\_prop</sub> showed overall improvement in EC quality compared to EC<sub>two</sub>.

### 6.3.2 Computational performance

To evaluate the computational performance of the proposed three-material model, we compared the processing time of the proposed model (i.e., EC<sub>three\_prop</sub>) to that of

the previous three-material model (i.e.,  $EC_{\text{three\_prev}}$ ) [36]. For the previous three-material model, we generated the code-book by uniformly sampling the model representation in material fraction space. When considering the relationship between the sampling rate of code-book generation and the processing time for the comparison of all of the entries in the code-book, the sampling rate should be set to allow a fair comparison between  $EC_{\text{three\_prev}}$  and  $EC_{\text{three\_prop}}$ . In  $EC_{\text{two}}$  and  $EC_{\text{three\_prop}}$ , the orthogonal projection for the two-material model was solved in an iterative manner until the change of the material fractions of less than 0.01 is achieved. Thus, for a fair comparison between  $EC_{\text{three\_prev}}$  and  $EC_{\text{three\_prop}}$ , the sampling rate for the generation of code-book in  $EC_{\text{three\_prev}}$  was also set as 0.01.

The processing time of each method was averaged over 10 runs to all the datasets.  $EC_{\text{three\_prev}}$  required 0.04 s for the generation of code-book in the pre-processing step, which could be saved in  $EC_{\text{three\_prop}}$ . For the estimation of three-material fractions of T-junction voxels,  $EC_{\text{three\_prev}}$  took about 30 s since the data measurement triplet at each voxel should be compared with every entry in the code-book to find the best match that yields the minimum least square error. On the other hand,  $EC_{\text{three\_prop}}$  reduced the processing time for the estimation of three-material fractions to 6 s, thus resulting in a speed up 5 times.

## Chapter 7. Conclusion

In this paper, we proposed a new ST-preserving EC method for removing TMs in CT images, while preserving folds and polyps submerged in the TMs. Unlike most previous EC methods that mitigate the PV effect by estimating material fractions and using this information to reconstruct CT density values, the proposed EC method reconstructs the CT density values using both material fractions and structural responses. In our approach, colonic components including air, TM,  $IL_{air/TM}$ ,  $IL_{ST/TM}$ , and T-junction are segmented respectively. For each voxel in the segmented  $IL_{ST/TM}$  and T-junction, the two- and three-material fractions at the voxel are derived using a two- and three-material transition models, respectively. The structural response is also calculated by rut- and cup-enhancement functions based on the eigenvalue signatures of the Hessian matrix. Then, the CT density value of each voxel in  $IL_{ST/TM}$  and T-junction is reconstructed based on the material fractions and the structural response at the voxel, whereas voxels in TM and  $IL_{air/TM}$  are simply replaced with air. As our ST-preserving EC model integrates the structural response into the material fractions-based reconstruction model, erroneous cleansing of submerged folds and polyps due to the PEH effect, which is one of most common limitations of previous EC methods, can be mitigated.

To reduce the computational complexity of solving the orthogonal projection problem in the three-material transition model, we currently propose a projection for the three-material model that provides a very quick estimate of the three-material fractions without the use of code-book, which is pre-generated by uniformly sampling the model representation in material fraction space and used to

find the best match with the observed measurements. In our simplified three-material model, three pairs of two-material fractions are calculated by using the two-material transition model and then simply combined into a single triple of three-material fractions based on the barycentric interpolation in material fraction space.

The experimental results using 10 clinical CT datasets demonstrated that the shape and texture information of submerged folds were better preserved with  $EC_{\text{our}}$  than with  $EC_{\text{prev}}$ . Compared to  $EC_{\text{prev}}$ ,  $EC_{\text{our}}$  showed overall higher grades of the cleansing quality for tagged pools in subjective evaluation. In addition, in terms of the accuracy of polyp detection after EC, the number of false-positive detections was slightly reduced in  $EC_{\text{our}}$  than in  $EC_{\text{prev}}$  while the sensitivity of polyp detection was identical to each other. In objective evaluation, the better preservation of submerged folds in  $EC_{\text{our}}$  was also supported by higher mean density values and fold preservation rates for the manually segmented folds. In addition, by using the fast projection for the three-material model,  $EC_{\text{our}}$  clearly reconstructed the whole colon surface including without the T-junction artifacts, which are observed as distracting ridges along the line where the  $IL_{\text{air/TM}}$  touches the colon surface when the two-material model does not cope with the three-material fractions at T-junctions.

## Bibliography

- [1] N. C. I. C. o. Korea. "Cancer Facts & Figures 2012 in the Republic of Korea,"  
[http://www.cancer.go.kr/mbs/cancer/subview.jsp?id=cancer\\_040201000000](http://www.cancer.go.kr/mbs/cancer/subview.jsp?id=cancer_040201000000).
- [2] A. C. Society, *Cancer Facts & Figures 2013*, 2013.
- [3] M. O'Brien *et al.*, "The national polyp study. Patient and polyp characteristics associated with high-grade dysplasia in colorectal adenomas," *Gastroenterology*, vol. 98, no. 2, pp. 371-379, Feb., 1990.
- [4] Z. Wang *et al.*, "An improved electronic colon cleansing method for detection of colonic polyps by virtual colonoscopy," *IEEE Trans. Biomed. Eng.*, vol. 53, no. 8, pp. 1635-1646, Aug., 2006.
- [5] W. I. Wolff *et al.*, "Colonofiberoscopy," *The Journal of the American Medical Association*, vol. 217, no. 11, pp. 1509-1512, Sep., 1971.
- [6] A. E. Kaufman *et al.*, "Virtual colonoscopy," *Commun. ACM*, vol. 48, no. 2, pp. 37-41, Feb., 2005.
- [7] S. Dogramadzi *et al.*, "Computer controlled colonoscopy," in *IEEE Instrument Measurement Technology Conference (IMTC)*, St. Paul, MN, USA 1998, pp. 210-213.

- [8] Z. Liang *et al.*, “Virtual colonoscopy versus optical colonoscopy,” *Expert Opinion on Medical Diagnostics*, vol. 4, no. 2, pp. 159-169, Mar., 2010.
- [9] A. S. F. G. Endoscopy, “Appropriate use of gastrointestinal endoscopy,” *Gastrointestinal Endoscopy*, vol. 52, no. 6, pp. 831-837, 2000.
- [10] C. I. Bartram, “Bowel preparation — Principles and practice,” *Clinical Radiology*, vol. 49, no. 6, pp. 365-367, June, 1994.
- [11] S. D. Wexner *et al.*, “A consensus document on bowel preparation before colonoscopy: Prepared by a Task Force From The American Society of Colon and Rectal Surgeons (ASCRS), the American Society for Gastrointestinal Endoscopy (ASGE), and the Society of American Gastrointestinal and Endoscopic Surgeons (SAGES),” *Gastrointestinal Endoscopy*, vol. 63, no. 7, pp. 894-909, June, 2006.
- [12] L. E. Smith, “Fiberoptic colonoscopy: Complications of colonoscopy and polypectomy,” *Diseases of the Colon & Rectum*, vol. 19, no. 5, pp. 407-412, Jul.-Aug., 1976.
- [13] G. W. Stevenson *et al.*, “Pain following colonoscopy: Elimination with carbon dioxide,” *Gastrointestinal Endoscopy*, vol. 38, no. 5, pp. 564-567, Sep.-Oct., 1992.
- [14] P. Orsoni *et al.*, “Colonic perforation due to colonoscopy: A retrospective study of 48 cases,” *Endoscopy*, vol. 29, no. 3, pp. 160-164, Mar., 1997.



- [15] B. Bressler *et al.*, “Colonoscopic miss rates for right-sided colon cancer: A population-based analysis,” *Gastroenterology*, vol. 127, no. 2, pp. 452-456, Aug., 2004.
- [16] P. J. Pickhardt *et al.*, “Location of Adenomas Missed by Optical Colonoscopy,” *Annals of Internal Medicine*, vol. 141, no. 5, pp. 352-359, Sep., 2004.
- [17] D. Heresbach *et al.*, “Miss rate for colorectal neoplastic polyps: A prospective multicenter study of back-to-back video colonoscopies,” *Endoscopy*, vol. 40, no. 4, pp. 284-290, Apr., 2008.
- [18] C. G. Coin *et al.*, “Computerized radiology of the colon: A potential screening technique,” *Comput. Radiol.*, vol. 7, no. 4, pp. 215-221, Jul.-Aug., 1983.
- [19] L. H. Shigeru *et al.*, “Virtual voyage: Interactive navigation in the human colon,” in *ACM SIGGRAPH*, 1997, pp. 27-34.
- [20] J. T. Ferrucci, “Colon cancer screening with virtual colonoscopy: Promise, polyps, politics,” *Am. J. Roentgenol.*, vol. 177, no. 5, pp. 975-988, Nov., 2001.
- [21] M. M. Morrin *et al.*, “Screening virtual colonoscopy—Ready for prime time?,” *N. Engl. J. Med.*, vol. 349, no. 23, pp. 2261-2264, Dec., 2003.
- [22] L. Hong *et al.*, “Reconstruction and visualization of 3D models of colonic surface,” *IEEE Trans. Nucl. Sci.*, vol. 44, no. 3, pp. 1297-1302, Jun., 1997.

- [23] I. Serlie *et al.*, “Improved visualization in virtual colonoscopy using image-based rendering,” in Joint Eurographics-IEEE TCVG Symposium on Visualization, 2001, pp. 137-146.
- [24] A. K. Hara *et al.*, “Detection of colorectal polyps with CT colonography: Initial assessment of sensitivity and specificity,” *Radiology*, vol. 205, no. 1, pp. 59-65, Oct., 1997.
- [25] H. M. Fenlon *et al.*, “A comparison of virtual and conventional colonoscopy for the detection of colorectal polyps,” *N. Engl. J. Med.*, vol. 341, no. 20, pp. 1496-1503, Nov., 1999.
- [26] J. Yee *et al.*, “Colorectal neoplasia: Performance characteristics of CT colonography for detection in 300 patients,” *Radiology*, vol. 219, no. 3, pp. 685-692, Jun., 2001.
- [27] M. R. Callstrom *et al.*, “CT colonography without cathartic preparation: Feasibility Study,” *Radiology*, vol. 219, no. 3, pp. 693-698, Jun., 2001.
- [28] P. A. Lefere *et al.*, “Dietary fecal tagging as a cleansing method before CT colonography: Initial results—Polyp detection and patient acceptance,” *Radiology*, vol. 224, no. 2, pp. 393-403, Aug., 2002.
- [29] M. R. Wax *et al.*, “Electronic colon cleansing for virtual colonoscopy,” in 1st International Symposium on Virtual Colonoscopy, Boston, MA, USA, 1998, pp. 94.
- [30] D. Chen *et al.*, “A novel approach to extract colon lumen from CT images for virtual colonoscopy,” *IEEE Trans. Med. Imag.*, vol. 19, no. 12, pp. 1220-1226, Dec., 2000.

- [31] L. Li *et al.*, “An image segmentation approach to extract colon lumen through colonic material tagging and hidden Markov random field model for virtual colonoscopy,” in Proc. SPIE, San Diego, CA, USA, 2002, pp. 406-411.
- [32] S. Wang *et al.*, “An EM approach to MAP solution of segmenting tissue mixture percentages with application to CT-based virtual colonoscopy,” *Med. Phys.*, vol. 35, no. 12, pp. 5787-5798, Dec., 2008.
- [33] S. Lakare *et al.*, “3D digital cleansing using segmentation rays,” in IEEE Visualization, Salt Lake City, UT, USA, 2000, pp. 37-44.
- [34] M. E. Zalis *et al.*, “Digital subtraction bowel cleansing for CT colonography using morphological and linear filtration methods,” *IEEE Trans. Med. Imag.*, vol. 23, no. 11, pp. 1335-1343, Nov., 2004.
- [35] I. W. O. Serlie *et al.*, “Classifying CT image data into material fractions by a scale and rotation invariant edge model,” *IEEE Trans. Image Process.*, vol. 16, no. 12, pp. 2891-2904, Dec., 2007.
- [36] I. W. O. Serlie *et al.*, “Electronic cleansing for computed tomography (CT) colonography using a scale-invariant three-material model,” *IEEE Trans. Biomed. Eng.*, vol. 57, no. 6, pp. 1306-1317, Jun., 2010.
- [37] M. Franaszek *et al.*, “Hybrid segmentation of colon filled with air and opacified fluid for CT colonography,” *IEEE Trans. Med. Imag.*, vol. 25, no. 3, pp. 358-368, Mar., 2006.

- [38] W. Cai *et al.*, "Structure-analysis method for electronic cleansing in cathartic and noncathartic CT colonography," *Med. Phys.*, vol. 35, no. 7, pp. 3259-3277, Jul., 2008.
- [39] W. Cai *et al.*, "Mosaic decomposition: An electronic cleansing method for inhomogeneously tagged regions in noncathartic CT colonography," *IEEE Trans. Med. Imag.*, vol. 30, no. 3, pp. 559-574, Mar., 2011.
- [40] P. Perona *et al.*, "Scale-space and edge detection using anisotropic diffusion," *IEEE Trans. Pattern Anal. Mach. Intell.*, vol. 12, no. 7, pp. 629-639, Jul., 1990.
- [41] G. Iordanescu *et al.*, "Automated seed placement for colon segmentation in computed tomography colonography," *Acad. Radiol.*, vol. 12, no. 2, pp. 182-190, Feb., 2005.
- [42] R. Lumia, "A new three-dimensional connected components algorithm," *Comput. Vision Graph.*, vol. 23, no. 2, pp. 207-217, Aug., 1983.
- [43] Q. Hu *et al.*, "Fast connected-component labelling in three-dimensional binary images based on iterative recursion," *Comput. Vis. Image Und.*, vol. 99, no. 3, pp. 414-434, Sep., 2005.
- [44] S. R. Sternberg, "Biomedical image processing," *IEEE Computer*, vol. 16, no. 1, pp. 22-34, Jan., 1983.
- [45] G. Kindlmann *et al.*, "Semi-automatic generation of transfer functions for direct volume rendering," in *IEEE Symposium on Volume Visualization*, Research Triangle Park, NC, USA, 1998, pp. 79-86.

- [46] J. Kniss *et al.*, “Multidimensional transfer functions for interactive volume rendering,” *IEEE Trans. Vis. Comput. Graphics*, vol. 8, no. 3, pp. 270-285, Jul.-Sep., 2002.
- [47] H. Bouma *et al.*, “Correction for the dislocation of curved surfaces caused by the PSF in 2D and 3D CT images,” *IEEE Trans. Pattern Anal. Mach. Intell.*, vol. 27, no. 9, pp. 1501-1507, Sep., 2005.
- [48] I. W. O. Serlie *et al.*, *CT imaging characteristics*, 2006.
- [49] L. J. v. Vliet, “Grey-scale measurements in multi-dimensional digitized images,” Delft University, Netherlands, 1993.
- [50] S. S. Lee *et al.*, “Panoramic endoluminal display with minimal image distortion using circumferential radial ray-casting for primary three-dimensional interpretation of CT colonography,” *Eur. Radiol.*, vol. 19, no. 8, pp. 1951-1959, Aug., 2009.



## 초 록

대장 컴퓨터 단층 촬영 영상에서 조영 처리된 잔여물을 제거하기 위해 전자적 장세척 방법이 이용된다. 본 논문에서는 전자적 장세척 방법에서 결합의 주요 원인이 되는 부분 용적 효과와 가성 상승 효과를 동시에 해결하기 위해 물질 혼합비율과 구조적 특징의 통합 재구성 모델을 이용한 전자적 장청소 기법을 제안한다. 먼저 대장 컴퓨터 단층 촬영 영상에서 공기, 조영 처리된 잔여물, 공기와 조영 처리된 잔여물 사이의 경계 (공기-잔여물 경계), 대장외부의 연조직과 조영 처리된 잔여물 사이의 경계 (연조직-잔여물 경계), 그리고 공기, 연조직, 조영 처리된 잔여물이 만나는 경계 (공기-연조직-잔여물 경계) 영역을 포함한 결합 요소를 분할한다. 분할된 공기와 공기-잔여물 경계 영역에 대해서는 각 복셀의 밀도값을 동일하게 공기의 대표 밀도값으로 대체함으로써 잔여물을 제거한다. 반면에 분할된 연조직-잔여물 경계와 공기-연조직-잔여물 경계 영역에 대해서는 물질 혼합비율과 구조적 특징을 계산한다. 물질 혼합비율은 두 물질간 혹은 세 물질간 전이 모델을 이용하여 예측하고 구조적 특징은 헤시안 행렬의 아이겐 분석에 기반하여 계산한다. 계산된 물질 혼합비율과 구조적 특징을 이용하여 연조직-잔여물 경계와 공기-연조직-잔여물 경계 영역에 속하는 각 복셀의 밀도값이 재구성된다. 물질 혼합비율과 구조적 특징의 통합 재구성 모델은 각 복셀 내의 연조직의 부분 용적을 유지시키는 동시에 조영 처리된 잔여물의 가성 상승 효과로 인해 약화된 잔여물에 잠긴 대장 주름 및 용종이 보존될 수 있도록 한다. 따라서 제안된 전자적 장세척 방법에서는 부분 용적 효과로 인한 연조직-잔여물 경계의 계단무늬 결합과 가성 상승 효과로 인한 잔여물에 잠긴 대장 주름 및 용종의 지나친 세척 결합을 피할 수 있다. 또한 본 논문에서는 기존 세 물질간 전이 모델의 연산

복잡도를 줄이기 위해 단순 세 물질간 전이 모델을 제안한다. 단순 세 물질간 전이 모델에서는 두 물질간 전이 모델을 반복 적용시킴으로써 얻어진 세 쌍의 (공기-연조직, 공기-잔여물, 연조직-잔여물) 두 물질간 혼합비율을 구하고 이를 삼각형을 이용한 무게중심좌표 상에서의 보간 방법을 이용해 하나의 세 물질간 혼합비율로 변환한다. 열개의 임상 데이터를 이용하여 제안한 전자적 장세척 방법의 성능을 평가하였다. 방사선 전문의에 의한 장세척 품질 평가에서 제안 방법이 물질 혼합비율을 이용한 기존 방법에 비해 더 높은 점수의 장세척 결과를 보였으며, 특히 잔여물에 잠긴 대장 주름 및 용종이 더 잘 보존되는 것을 확인하였다. 이러한 결과는 잔여물에 잠긴 대장 주름 영역을 수동 분할하여 제안 방법과 기존 방법에 의한 장세척 결과 영상에서 해당 영역의 평균 밀도값과 주름 보존 비율을 비교한 결과에서도 마찬가지로 입증되었다. 또한 기존의 두 물질간 전이 모델로는 잘 해결되지 않았던 공기-연조직-잔여물 경계 영역에서의 산등성이 형태의 결함에 대해서도 제안 방법에서는 단순 세 물질간 전이 모델을 이용하여 공기-연조직-잔여물 경계 영역에서의 결함을 제거하고 전체 대장의 표면이 깨끗하게 재구성되는 것을 확인하였다.

주요어: 전자적 장세척, 물질 혼합비율, 구조적 특징, 대장 가상

내시경

학번: 2009-30208